12 Light Control of Many-Body Phases

Matteo Mitrano
Harvard University, Department of Physics
17 Oxford Street, 02138 Cambridge (MA)

Contents

E. Pavarini and E. Koch (eds.)
Correlated Materials: Methods and Applications
Modeling and Simulation Vol. 16, Forschungszentrum Jülich, 2026
ISBN 978-3-95806-909-1 http://www.cond-mat.de/events/correl26

1 Introduction

This chapter is devoted to the use of the light-matter interaction to coherently engineer many-body states in quantum materials. Ultrashort optical fields have enabled advances in the manipulation of quantum states in solids and in the discovery of emergent phenomena out of equilibrium [1–5]. Light now stands alongside doping, gating, strain, and pressure as a tuning knob for material properties, and is increasingly used as a tool to synthesize novel states of matter.

The field of *photoinduced phase transitions* has been shaped by the recognition that light can do more than heat a material or incoherently excite quasiparticles. In systems governed by a subtle balance of competing electronic interactions, optical excitation can trigger colossal cooperative responses. Early demonstrations established the central idea that prompt photoexcitations can nucleate macroscopic changes of electronic and structural order [6]. Driven by advances in tunable laser sources, the field has moved from the study of melting, thermalization, and structural responses [7] toward the implementation of coherent control protocols in which tailored optical fields are used to modify Hamiltonians, coherently manipulate ordered states, and access nonequilibrium states without direct equilibrium analogs.

In the following, we focus primarily on experiments aimed at *controlling* material properties. There is a vast literature in which nonequilibrium techniques are used to perturb solids and study near-equilibrium properties. Our primary interest is instead in emergent phenomena and functionalities induced by light in strongly interacting electron systems [5, 8], although we will occasionally discuss systems better described as weakly interacting electron ensembles. Experiments involving optical dressing in cavities will be discussed only in the outlook, as this exciting and rapidly developing direction lies beyond the scope of this chapter.

To keep the chapter focused, we discuss only selected key experimental achievements, together with high-level aspects of the theory, and refer the reader to the literature where appropriate.

2 Experimental techniques

Progress in the light control of quantum materials is closely tied to the development of new laser sources and experimental probes. Most light-control experiments rely on a pump-probe protocol: an intense optical field, the *pump*, drives a material out of equilibrium and toward a desired quantum state, while a delayed and typically weaker pulse, the *probe*, interrogates the properties of the transient state. The measurement is repeated stroboscopically when the system relaxes back to equilibrium between successive pump pulses, or performed in single-shot mode when materials undergo irreversible transitions.

Early experiments relied on a comparatively limited set of optical excitation conditions. The development of ultrafast light sources that reliably generate intense pulses from the terahertz to the extreme ultraviolet, with tunable pulse duration, polarization, bandwidth, and repetition rate [9–13], has opened a much more selective approach to driving quantum materials. Optical fields can now be matched to specific electronic transitions, coupled directly to collective modes, or tuned into transparency regions to minimize incoherent excitation processes. It is this selectivity that turns light from an external perturbation into a control field.

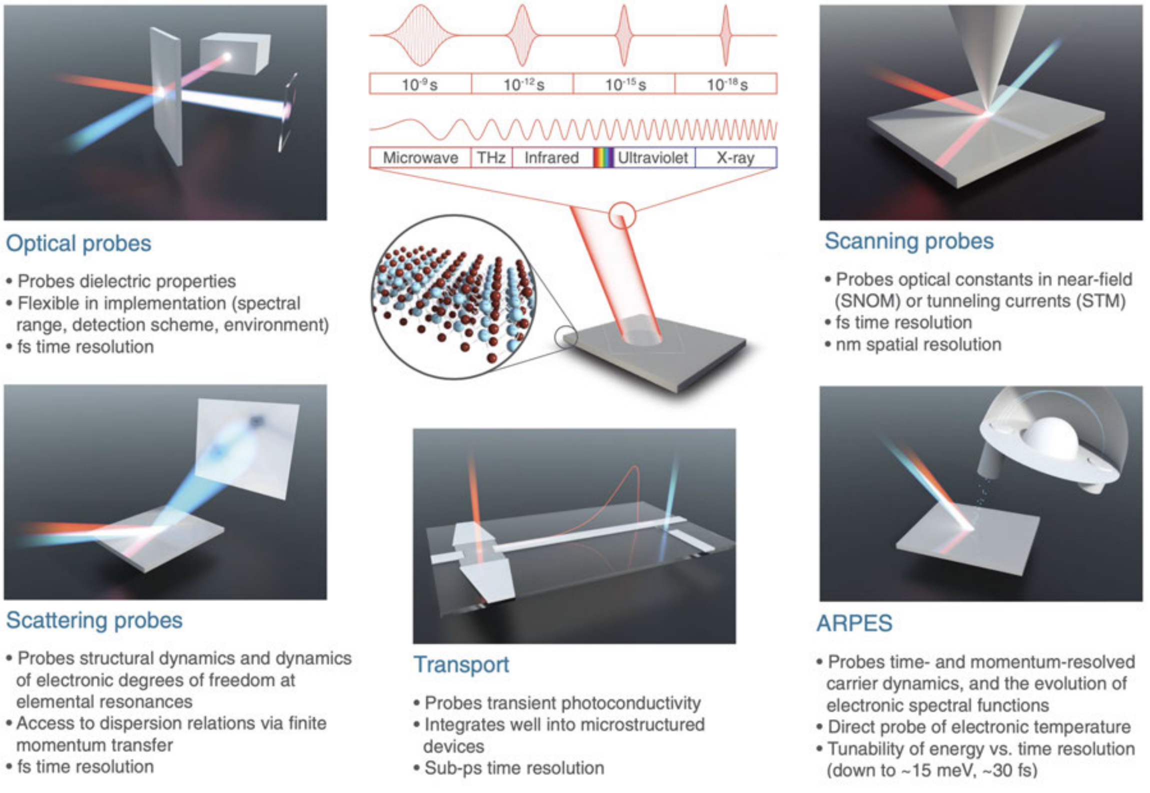

Fig. 1: *Overview of experimental techniques used to study optically driven quantum materials. The upper central panel shows the spectral regions and timescales of ultrafast pulses commonly used to drive materials out of equilibrium. The surrounding panels show time-resolved probes with complementary spatial, energy, and momentum resolution. Reprinted figure with permission from Ref. [4]. Copyright (2022) by the American Physical Society.*

These developments have occurred in tandem with a gradual expansion of the experimental probe toolkit. This section introduces several experimental techniques that will facilitate the discussion in the rest of the chapter (Fig. 1). The first, and most widely used, is *time-resolved optical spectroscopy*. Since part of the laser output is used to generate the pump pulse, another fraction can often be used to interrogate the time-dependent optical properties of the material [14]. This broad family of experiments encompasses many techniques and observables, ranging from transient absorption and reflectivity measurements to track the redistribution of spectral weight that accompanies a change of electronic state [15–19] to polarization-rotation experiments measuring the magnetization in magnetic systems [20]. Extending time-resolved optical experiments from the visible into the terahertz (THz) range gives the most direct access to the low-energy electrodynamics of correlated systems, charge-density-wave states, and superconductors [21], where the relevant gaps and collective modes reside. Second- and third-harmonic polarimetry, in turn, is sensitive to the local symmetry of the lattice [22, 23] and has been used to probe ordered states in and out of equilibrium [24–26].

A second major experimental tool is time- and angle-resolved photoemission spectroscopy (trARPES) [27]. In this technique, ultrafast XUV photons (generated either by cascaded upconversion of the fundamental laser wavelength or by high-harmonic generation) impinge on a material and trigger electron emission through the photoelectric effect. Detection of the emitted electrons provides momentum- and energy-resolved access to the single-particle spectral function. This technique is essential for tracking band structure changes in optically-driven materials and detecting nonthermal regimes far from equilibrium [28]. It has been used to study decoherence [29], the coupling of electrons to other degrees of freedom [30], and the dynamics of gaps and quasiparticles in high-temperature superconductors [31] and charge-density-wave states [32, 33]. Remarkably, trARPES has also provided some of the clearest visualizations of Floquet-Bloch states to date [34–37]. Finally, momentum microscopes are enabling photoemission studies of two-dimensional materials and devices over multiple Brillouin zones.

A third major class of experimental methods are time-resolved x-ray and electron scattering. The development of femtosecond x-ray sources, particularly x-ray free-electron lasers (XFELs) [38], together with ultrafast electron sources operating from the keV to MeV range [39], has enabled scattering experiments in which the probe wavelength is comparable to interatomic distances. Time-resolved x-ray and electron diffraction provide direct access to structural dynamics [40, 41] and are especially sensitive to phase transitions in which electronic degrees of freedom are coupled to lattice distortions [42–47]. In parallel, resonant x-ray techniques have extended this approach beyond structural probes. By tuning the photon energy to elemental absorption edges, time-resolved x-ray absorption (trXAS) and resonant inelastic x-ray scattering (trRIXS) can selectively track charge, spin, orbital, and lattice degrees of freedom in optically driven materials [48, 49]. With the introduction of high-resolution spectrometers at XFELs, trRIXS is becoming an increasingly effective discovery tool for novel states of matter.

Finally, the increasing relevance of two-dimensional materials, heterostructures, and devices has motivated the development of local and device-integrated time-resolved probes. Time-resolved scanning tunneling microscopy (STM) accesses ultrafast tunneling dynamics with atomic-scale spatial sensitivity [50, 51], while time-resolved scanning near-field optical microscopy (trSNOM) probes transient optical constants with nanometer resolution [52]. These techniques are especially valuable when photoinduced states are spatially inhomogeneous, confined to surfaces or interfaces, or embedded in mesoscopic structures. In parallel, ultrafast transport measurements have emerged as a complementary route to nonequilibrium dynamics, providing direct access to transient photoconductivity, photocurrents, and light-induced changes in device response [53]. These local methods are decisive when the photoinduced state is spatially inhomogeneous, and together with the optical, photoemission, and scattering probes above they form the toolkit used throughout this chapter.

3 Photoinduced insulator-to-metal transitions

Photoinduced insulator-to-metal transitions are a natural starting point for understanding nonequilibrium phenomena in correlated solids [54, 55]. The equilibrium state is characterized by a single, well-defined quantity, the charge gap, and decades of equilibrium work provide a firm benchmark for experiments far from equilibrium. We first introduce Mott-Hubbard and charge-transfer insulators, and then examine the incoherent and coherent pathways by which light turns an insulator into a metal.

Every photoinduced transition shares a common sequence of events: light couples to a fast subsystem, usually the electrons, which in turn drives the slow variables that define a phase, such as a lattice distortion, an order parameter, or a magnetization [6]. What separates the two pathways is whether this drive preserves phase information or merely deposits energy into the target. In an incoherent process the absorbed energy dephases among the fast carriers faster than the slow variables can respond. The excitation then acts as a sudden reshaping of the free-energy landscape, and the material reaches a new state through relaxation, dissipation, and nucleation. A coherent process instead channels energy into a specific collective coordinate, driving it with a well-defined phase and with damping slower than its period, so that the system evolves along a controlled, often oscillatory, trajectory rather than by relaxation. The distinction is properly defined with respect to the slow variables, since an incoherent electronic excitation can itself set a lattice mode ringing coherently. Because they inject little entropy, coherent excitation processes are more selective, energy-efficient and tunable, and they make light a genuine control field rather than a source of heat.

3.1 Mott-Hubbard and charge-transfer insulators

The physics of strongly correlated materials is governed by the competition between electronic delocalization and Coulomb-driven localization [56, 57]. When electron-electron interactions become comparable to the kinetic energy, the motion of each carrier is no longer independent and becomes constrained by the configuration of the other valence electrons. A minimal Hamiltonian capturing this competition is the extended Hubbard model,

$$H = -t\sum_{i\sigma}\left(c^{\dagger}_{i\sigma}c_{i+1\sigma} + H.c.\right) + U\sum_{i} n_{i\uparrow}n_{i\downarrow} + V_1\sum_{i} n_i n_{i+1} + V_2\sum_{i} n_i n_{i+2} + \cdots\,, \quad (1)$$

where $c^{\dagger}_{i\sigma}$ and $c_{i\sigma}$ create and annihilate an electron with spin σ on lattice site i, $n_{i\sigma} = c^{\dagger}_{i\sigma}c_{i\sigma}$, and $n_i = n_{i\uparrow}+n_{i\downarrow}$. The hopping amplitude t sets the kinetic energy scale, while U describes the on-site Coulomb repulsion between two electrons occupying the same site. The terms $V_1, V_2, \ldots$ account for longer-range Coulomb interactions between electrons on nearest-neighbor, next-nearest-neighbor, and more distant sites. The corresponding electronic bandwidth is $W = 2zt$, where z is the number of nearest neighbors.

When only the on-site Coulomb interaction is retained, the resulting simple Hubbard model is governed primarily by two parameters, the number of electrons per site (*filling*), and the interaction ratio U/W (*Mottness*). The essential physics of the half-filled Hubbard model is already contained in its two exactly solvable limits. For $U = 0$ the model reduces to a tight-binding band which, being half filled, describes a metal. In the opposite atomic limit $t = 0$ every site is singly occupied, intersite transport is blocked by the Coulomb penalty U, and the ground state is a Mott insulator (see Fig. 2). Tuning U/W between these limits drives a metal-to-insulator transition. The spectrum splits into a lower and an upper Hubbard band separated by a charge gap of order U, which measures the energy cost of creating an empty site (*holon*) and a

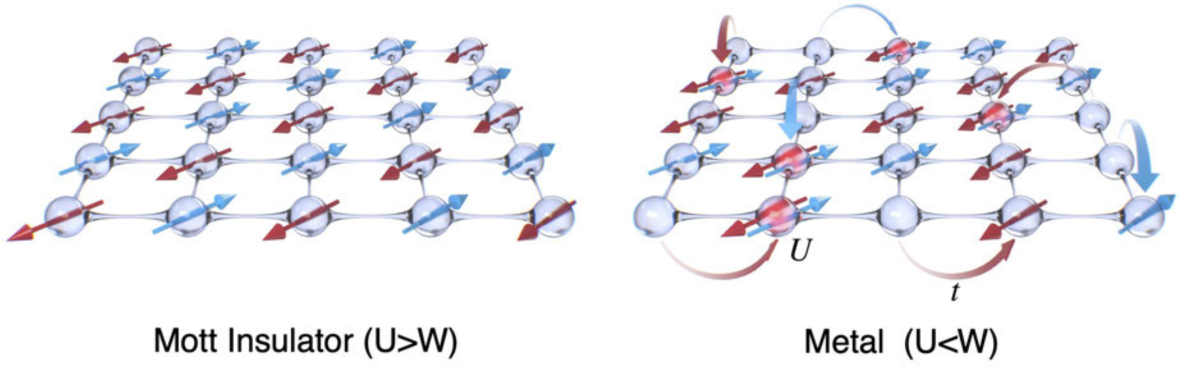

Fig. 2: *Correlated electron dynamics in a square lattice at half filling. When the on-site Coulomb repulsion U is larger than the electron bandwidth W, the electrons localize and form a Mott insulating state. In the opposite limit ($U < W$), they transition into a metallic state.*

doubly occupied one (*doublon*). Spin degrees of freedom introduce an additional energy scale. Virtual hopping onto a neighboring occupied site and back lowers the energy of antiparallel spins, generating an antiferromagnetic superexchange $J = 4t^2/U$. Charge and spin are thus controlled by two widely separated scales, $U \gg J$.

In real materials the gap is not always set by the Hubbard U. Following Zaanen, Sawatzky, and Allen [58], one distinguishes Mott-Hubbard insulators, where the gap separates the lower and upper Hubbard bands ($\sim U$), from charge-transfer insulators, where the lowest charge excitation moves an electron from a filled ligand band onto the correlated site, so that the gap is set by the charge-transfer energy $\Delta < U$. Most transition-metal oxides of interest, including cuprates and nickelates, belong to the charge-transfer class, a distinction that is relevant for determining which excitations are addressed by the optical pump.

3.2 Incoherent excitation processes and photodoping

The simplest incoherent process for inducing an insulator-to-metal transition with light is the injection of mobile charge carriers across the gap. In a half-filled Mott insulator, photons with energies comparable to or larger than the on-site interaction U can delocalize charges between neighboring sites, creating holon-doublon pairs and thereby driving a transient insulator-to-metal transition. Although this mechanism (often referred to as *photodoping*) resembles chemical doping in the introduction of mobile charges, photoinduced metallic states may host multiple types of carriers, nonthermal distributions, and emergent dynamic phenomena.

A compelling example is the one-dimensional Mott insulator (BEDT-TTF)-F_2TCNQ. This molecular solid hosts chains of BEDT-TTF molecules and is characterized by weak electron-lattice coupling and the absence of a Peierls distortion. Okamoto *et al.* investigated its response by pumping along the BEDT-TTF chains with 1.55 eV photons [59], well above the 700 meV Mott gap, and probing the optical response over the 0.08-2.5 eV range (Fig. 3). Immediately after photoexcitation, the reflectivity associated with the Mott gap is depleted, while the low-

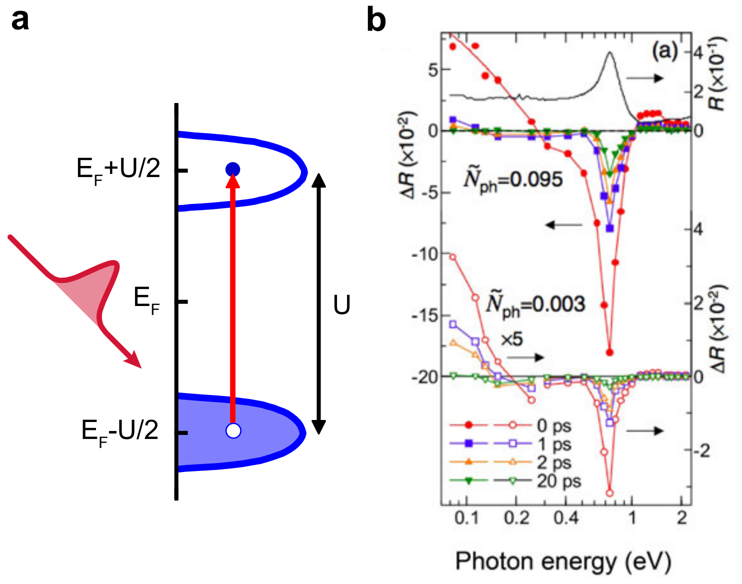

Fig. 3: *Photoinduced insulator-to-metal transition in (BEDT-TTF)-F$_2$TCNQ.* ***a*** *Sketch of photodoping of a Mott insulator. The pump excites electrons from the lower Hubbard band at $E_F - U/2$ (E_F, Fermi energy) into the upper Hubbard band at $E_F + U/2$.* ***b*** *Transient reflectivity changes $\Delta R = R(t) - R_{eq}$ along the a-axis after photoexcitation with 1.55 eV photons with 0.095 photons/ET molecule and 0.003 photons/ET molecule excitation densities. Adapted with permission from Ref. [59]. Copyright (2007) by the American Physical Society.*

energy reflectivity below roughly 200 meV increases, signaling gap melting and transient metallization. The transient reflectivity change $\Delta R(t)$ follows a double-exponential relaxation and recovers within approximately 2 ps. Subsequent experiments showed that holon-doublon pairs exhibit quantum interference between bound and unbound states at early times [60], and that their relaxation times depend sensitively on the degree of electronic correlation [61]. This example illustrates a largely electronic route to transient metallization, in which the insulating state is destabilized by photocarrier injection without evidence for a structural phase transition. Similar organics also support the reverse process. In metallic α-(BEDT-TTF)$_2$I$_3$, a 1.5-cycle near-infrared pump pulse (7 fs, 9.3 MV cm^{-1}, 0.6–0.95 eV) has been shown to drive a transient metal-to-insulator transition, tracked by broadband reflectivity resolved in energy and delay [62]. The field lowers the hopping t by roughly 10% through dynamical localization, opening a gap associated with charge order. Photoinduced metallization has also been observed in other charge-transfer insulators, including two-dimensional copper oxides [63, 64].

While the discussion so far has emphasized electronic dynamics, lattice degrees of freedom can play several important roles as relaxation channels for holon-doublon pairs, as drivers of polaronic resonances, or as cooperative variables in the photoinduced response. In some materials, electronic and structural degrees of freedom are so strongly intertwined that the photoinduced insulator-to-metal transition is accompanied by a proper structural phase transition. A paradigmatic case is that of vanadium dioxide, VO_2.

At equilibrium, VO_2 exhibits a sharp insulator-to-metal transition accompanied by a structural change from a low-temperature monoclinic phase (M1), characterized by dimerized V–V chains, to a high-temperature rutile phase (R), with undimerized V–V bonds [65]. Ultrafast optical pulses can similarly switch VO_2 from an insulating to a metallic state, and this photoinduced transition is accompanied by a monoclinic-to-rutile structural transition. A series of pump-probe experiments using 1.55 eV excitation have examined the relative roles of electronic and lattice degrees of freedom in this process [66,42,67,68,45]. Beyond identifying the primary driver of metallization, an important question is whether the accompanying structural transition is coherent or incoherent.

In a solid-solid transition where the crystal symmetry increases with temperature, as in the M1-to-R transition of VO_2, the structural response can occur either through a displacive or order-disorder mechanism. The VO_2 transition has long been interpreted as displacive, corresponding to a soft phonon mode of the high-symmetry metallic phase, based on symmetry arguments, diffraction measurements, and lattice-dynamics simulations. In this picture, the atoms collectively rearrange their positions along one or a few coherent vibrational coordinates that connect the low- and high-symmetry structures. Recent total x-ray scattering measurements, however, revealed diffuse scattering that is not expected for a purely displacive transition, but is characteristic of an order-disorder process [45]. These results indicate that the photoinduced insulator-to-metal transition in VO_2 is incoherent not only in its electronic dynamics, but also in the accompanying structural response.

3.3 Coherent control of the lattice and nonlinear phononics

We now turn to coherent pathways and discuss examples in which light is used to drive the lattice directly, rather than to inject carriers across the gap. Ultrashort pulses can coherently excite phonons through displacive excitation of modes whose equilibrium position shifts upon photoexcitation, or through impulsive stimulated Raman scattering [69,70]. These mechanisms, however, either rely on the excitation of electronic states or reach only a restricted set of Raman modes, and therefore offer limited tunability.

The development of intense, tunable sources in the mid-infrared and THz range has opened new excitation mechanisms, including the resonant driving of infrared-active vibrations to amplitudes large enough that lattice anharmonicity becomes essential (see Fig. 4a).

This connection is especially important in correlated oxides, where the crystal structure directly shapes electronic behavior. In ABO_3 perovskites, the transition-metal ion is coordinated by an oxygen octahedron, and even small rotations or tilts of these octahedra can reshape the electronic ground state. In manganites, for example, rotations of the MnO_6 octahedra modify the Mn–O–Mn bond angles, controlling the orbital overlap along the bonds and thereby the one-electron bandwidth W as well as the sign and magnitude of the exchange interactions. Hopping is maximal for a straight 180° bond and decreases as the bond bends. A vibration that periodically distorts these bonds therefore provides, in the language of the previous sections, a direct handle on U/W, and hence on the balance between insulating and metallic behavior.

This mechanism underlies the first vibrationally driven insulator-to-metal transition, reported by Rini *et al.* in the magnetoresistive manganite $Pr_{0.7}Ca_{0.3}MnO_3$ [72]. At low temperature, this

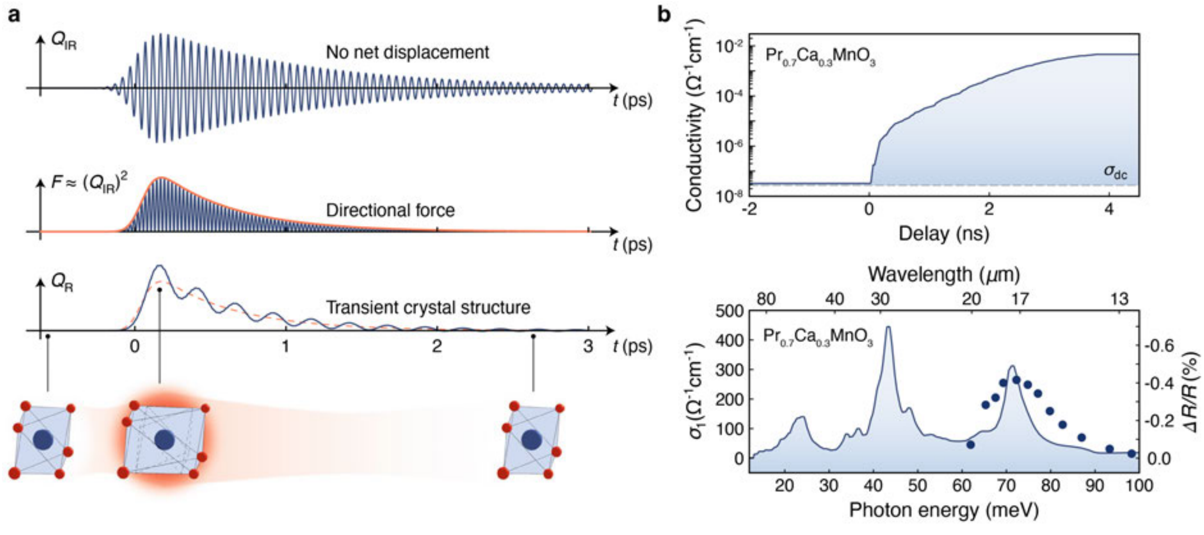

Fig. 4: *Nonlinear phononics and photoinduced insulator-to-metal transitions. (a) Nonlinear phononic response for an anharmonic coupling $V_{\rm anh} \propto Q_{\rm IR}^2 Q_R$, coherently driven infrared phonon amplitude (top), induced lattice force (middle), and resulting structural distortion along the Raman coordinate (bottom), together with a schematic distortion of a TMO_6 octahedron. (b) Transient resistivity increase in resonantly excited $Pr_{0.7}Ca_{0.3}MnO_3$ (top), and comparison of its equilibrium vibrational spectrum and resonant transient reflectivity response (bottom). Panels adapted with permission from Ref. [71]. Copyright (2021) by Springer Nature Limited. Data reproduced with permission from Ref. [72]. Copyright (2007) by Springer Nature Limited.*

compound is a charge- and orbital-ordered insulator. Resonant excitation of an infrared-active Mn–O stretching mode at 71 meV (17 THz) modulates the Mn–O–Mn bond angle, transiently broadening the electronic bandwidth and collapsing the gap. The resistivity drops by five orders of magnitude into a metastable metallic state (Fig. 4b). Unlike photodoping, no carriers are promoted across the gap and the lattice becomes the tuning knob of the electronic transition.

Driving a lattice mode to large amplitude is a general strategy whose systematic formulation is known as *nonlinear phononics* [73, 74, 71]. The essential physics can be captured by two anharmonically-coupled oscillators. An intense mid-infrared field resonantly drives an infrared-active mode $Q_{\rm IR}$ through its Born effective charge Z^*, while the lowest-order lattice anharmonicity, $V_{\rm anh} = g\, Q_{\rm IR}^2 Q_{\rm R}$, couples this motion to a Raman-active mode $Q_{\rm R}$

$$\ddot{Q}_{\rm IR} + \gamma_{\rm IR}\dot{Q}_{\rm IR} + \big(\omega_{\rm IR}^2 + 2g\, Q_{\rm R}\big) Q_{\rm IR} = Z^* E(t), \tag{2}$$

$$\ddot{Q}_{\rm R} + \gamma_{\rm R}\dot{Q}_{\rm R} + \omega_{\rm R}^2\, Q_{\rm R} = -g\, Q_{\rm IR}^2. \tag{3}$$

Because the driven infrared mode oscillates about zero, it does not by itself produce a net structural distortion. The quadratic term $Q_{\rm IR}^2$, however, generates a rectified force on $Q_{\rm R}$, displacing it toward a new quasi-equilibrium position and producing a coherent structural distortion along a selected Raman coordinate. This construction extends well beyond pairs of phonons, and in recent years it has been shown that the driven mode can couple anharmonically to magnetization, exchange and hopping integrals, or macroscopic strain, providing a symmetry-selective route to control both structural and electronic degrees of freedom (Table 1).

Table 1: *Nonlinear phononic processes and their effect on the structural and functional properties of a material, after Ref. [71].* Q_{driven}, *resonantly driven mode;* Q_c, *coupled phonon;* M, *magnetization;* $\mathbf{S}_i$, *local spin on site* i; U, *on-site Coulomb repulsion;* t, *hopping integral;* ε, *macroscopic strain.*

Nonlinearity	Effect
$Q^2_{\text{driven}} \cdot Q_c\,,\;\; Q_{\text{driven},1} \cdot Q_{\text{driven},2} \cdot Q_c$	Quasi-static lattice distortion
$\left(\mathbf{Q}_{\text{driven}} \times \mathbf{Q}_{\text{driven}}\right) \cdot M,\;\; Q^2_{\text{driven}}\, \mathbf{S}_i \cdot \mathbf{S}_j$	Change of magnetism
$Q^2_{\text{driven}} \cdot U,\;\; Q^2_{\text{driven}} \cdot t$	Change of electronic structure
$Q^2_{\text{driven}} \cdot \varepsilon$	Strain
$Q^4_{\text{driven}}\,,\;\; Q^2_{\text{driven}} \cdot Q_c^2,\; \ldots$	Phonon amplification, phonon squeezing

The reach of this approach extends beyond bulk excitation. A clear demonstration is provided by epitaxial thin films of the antiferromagnetic insulator $NdNiO_3$, whose metal-to-insulator transition is governed, as in the manganites, by the Ni–O–Ni bond angle and hence by the bandwidth [75]. In this experiment, a 33 nm film was grown on a $LaAlO_3$ substrate, and a 150 fs mid-infrared pulse was tuned not to a vibration of the film, but to the $\sim$15 µm ($\sim$80 meV) Al–O stretching mode of the *substrate*. Below the transition temperature, the driven substrate mode launches a lattice distortion that propagates across the interface and strains the nickelate, thus launching an insulator-to-metal transition. Spectral weight is transferred from high to low energy, and the quasi-dc conductivity of the film increases by five orders of magnitude within 3 ps. The metallic state is long-lived, with a lifetime exceeding 1 ns, while an estimated heating below 5 K rules out a thermal origin. The decisive evidence that the substrate is the active element is that the photosusceptibility of the transition follows the infrared absorption of $LaAlO_3$, rather than that of $NdNiO_3$. The heterostructure itself therefore becomes a design parameter, as changes in the substrate can be exploited to shift both resonance and magnitude of the response.

4 Light control of ordered states

In the previous section, we discussed transitions described by a single scalar quantity, the charge gap. We now turn to phenomena involving symmetry breaking and described by an *order parameter*, a quantity that vanishes in the symmetric state and acquires well-defined magnitude and phase once the symmetry is lowered. At equilibrium, lowering the temperature deforms the free energy until the symmetric minimum gives way to equivalent broken-symmetry minima. The system selects one of them, and transitions into a new ordered phase (Fig. 5a). Charge-density waves, antiferromagnets, and ferroelectrics are all manifestations of this physics, differing in the symmetry that is broken and in the microscopic nature of the order parameter.

Light can similarly manipulate ordered states in quantum materials. Intense pulses can drive the nonthermal melting of ordered phases, but can also, more interestingly, induce order far from equilibrium by coherently driving a quantum coordinate of the material (Fig. 5b). The frontier of the field lies in realizing nontrivial ordered states, possibly without equilibrium counterparts, and making them metastable after the excitation has decayed. In the following, we discuss examples of light control of ordered phases, such as charge order, magnetism, and ferroic orders.

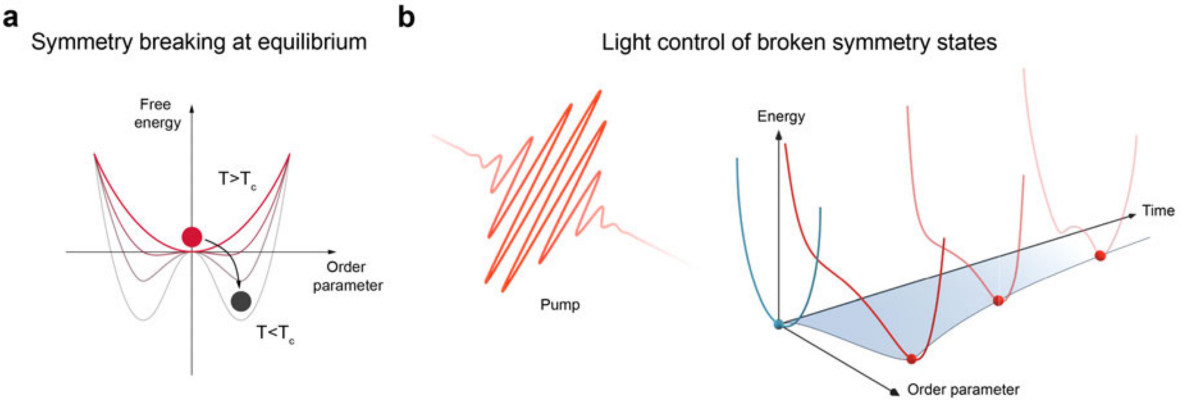

Fig. 5: *Symmetry breaking and its control with light. (a) At equilibrium, order emerges through spontaneous symmetry breaking. Lowering the temperature reshapes the free energy, creating equivalent broken-symmetry minima into which the system evolves from the high-symmetry configuration. (b) Pump pulses can reshape the free energy landscape in time and induce more ordered states. The evolving depth and position of the minima track the order parameter dynamics, with the goal of steering the system toward nontrivial, possibly metastable states.*

4.1 Charge-ordered phases

Charge-ordered phases form when valence electrons spontaneously self-organize into a spatially modulated state with a well-defined periodicity, often accompanied by a commensurate or incommensurate distortion of the lattice [76]. The order parameter is the complex amplitude $\eta = |\eta|e^{i\phi}$ of the density modulation, and its magnitude measures the strength of the order, while its phase ϕ fixes the position of the wave relative to the lattice. Such order parameter structure generally supports two characteristic collective excitations: amplitude, or amplitudon, fluctuations that modulate $|\eta|$, and phase, or phason, fluctuations of the modulation.

Charge-ordered states can be broadly grouped into two classes. In one, the order is driven by a structural Peierls-type instability, namely a periodic lattice distortion opens a gap at the Fermi surface, electronic and lattice modulations are locked together, and the amplitude mode can be identified, to a good approximation, with a lattice phonon. In the other, the modulation is primarily electronic, driven by Coulomb interactions and the kinetic frustration of charge carriers, with lattice distortions only playing a minor role. This distinction determines whether light excitation of the charge-ordered phase results in coherent lattice motion and structural rearrangements, or dynamics of the sole electronic subsystem. In practice, assigning a charge-ordered phase to one of these limits is often nontrivial [77], and the relative roles of electronic and lattice degrees of freedom remain widely debated. The classification used here should therefore be understood as an organizing principle rather than a sharp boundary.

Because charge order modulates the density on microscopic, often atomic, length scales, it is most directly accessed with momentum-resolved probes. trARPES tracks the opening and closing of the charge-order gap and the reconstruction of the single-particle spectral function, while time-resolved x-ray and electron scattering measure the superlattice reflections that directly fingerprint the modulation, giving access to its amplitude, periodicity, and correlation length.

As a first example, we return to charge- and orbital-ordered manganites, where charge order is intertwined with orbital and magnetic degrees of freedom. In $Pr_{1-x}Ca_xMnO_3$, localization of the Mn $3d$ electrons produces a coupled charge-orbital superlattice modulation, accompanied by a Jahn-Teller distortion of the MnO_6 octahedra. Beaud *et al.* used femtosecond x-ray diffraction to track the photoinduced melting of this order [43]. Although the structural transition involves many electronic and vibrational coordinates, they found that the photoinduced charge order melting is captured by a single time-dependent order parameter governed by the electronic excitation. Owing to the coupling to the lattice, photoexcitation also induces a strong coherent oscillation at $\sim$ 2.45 THz around the equilibrium positions of the higher-symmetry lattice.

The structural response is similarly strong in the quasi-1D Peierls insulator $K_{0.3}MoO_3$, the *blue bronze*, where the coherent oscillations represent the amplitude mode itself. Here the charge-density wave is a textbook periodic lattice distortion that opens a gap on a nested Fermi surface below $T_c = 183$ K. Huber *et al.* tracked the structural dynamics across the photoinduced charge-density-wave-to-metal transition with femtosecond x-ray diffraction [78]. At low excitation they followed coherent oscillations of the $\big(1, (4-q_b), 0.5\big)$ superlattice peak with a 1.7 THz frequency along the amplitude-mode coordinate, while above the melting threshold the periodic lattice distortion first collapsed and then transiently recovered according to the properties of the high-symmetry phase rather than those of the low-temperature phase. A photoemission study by Liu *et al.* resolved the same dynamics in the electronic structure, observing a 1.7 THz modulation of the bonding band as the signature of the amplitude mode, together with coherent phasons generated by the parametric amplification of phase fluctuations [79].

Similar cooperative responses of electronic and structural degrees of freedom are observed in layered transition-metal dichalcogenides. In these materials, the electronic modulation is accompanied by a commensurate structural supermodulation, with a wavelength that depends on the compound. In 1T-$TiSe_2$, Rohwer *et al.* used extreme-ultraviolet photoemission to image the band dispersion at large momenta and found that long-range charge order collapses within $\sim$20 fs, much faster than lattice motion, a speed attributed to transient screening of the electronic interaction by photogenerated carriers [32]. In the related compound 1T-TaS_2, a two-dimensional Mott insulator with commensurate charge order, Petersen *et al.* showed that the charge order, identified by the splitting of occupied subbands at the Brillouin-zone boundary, melts before the lattice responds [33]. Together, these results challenge a purely structural, Fermi-surface-nesting picture and point to a leading electronic role. Photoexcited 1T-TaS_2 can also enter a hidden metallic state with metastable character [80], making it one of the clearest examples of a light-induced quantum state inaccessible by equilibrium means.

In cuprate superconductors, charge order is largely electronic and tied to the formation of alternating stripes of holes and electrons in the CuO_2 planes [82, 83]. It is widely regarded as competing with superconductivity. In $La_{2-x}Ba_xCuO_4$ at $x = 1/8$ doping, this competition is the sharpest, as static stripe order suppresses bulk superconductivity, and possibly gives rise to a modulated phase known as pair density wave [84]. Early resonant x-ray scattering experiments showed a pump-induced suppression of the stripes under resonant vibrational excitation [85]. Mitrano *et al.* used time-resolved resonant soft x-ray scattering (elastic and in-

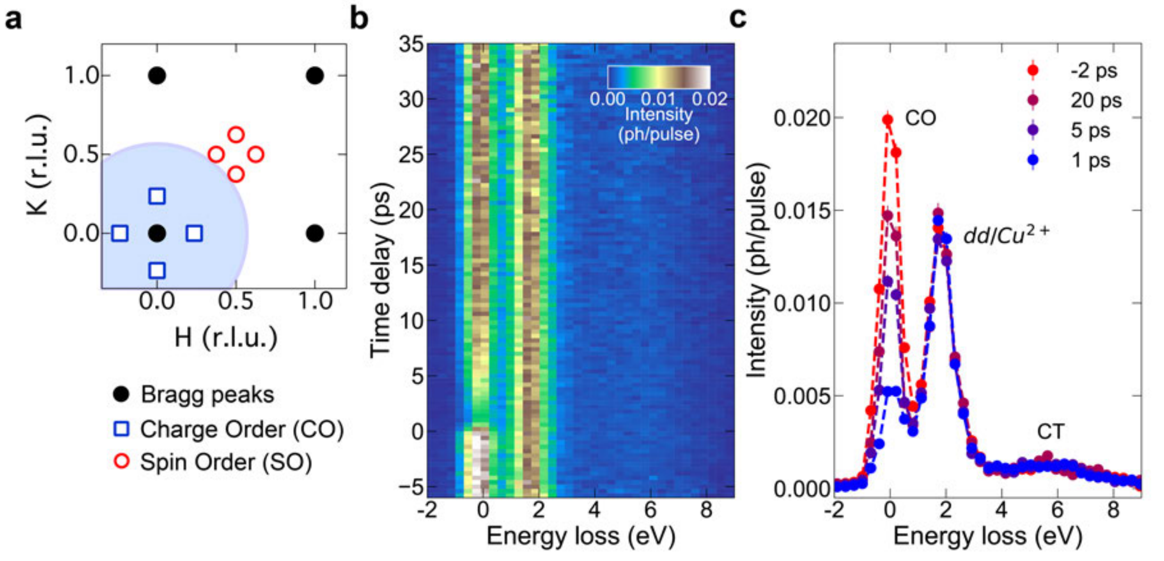

Fig. 6: *Ultrafast charge order melting in a cuprate superconductor. a. Reciprocal space map of structural, charge order (CO) and spin order (SO) peaks in $La_{2-x}Ba_xCuO_4$. The blue area represents the maximum momentum transfer achievable at the Cu L-edge (931 eV). b. Time-resolved resonant inelastic x-ray scattering (trRIXS) spectra at the Cu L-edge of photoexcited $La_{1.875}Ba_{0.125}CuO_4$ at $Q_{CO} = (0.236, 0, 1.5)$ r.l.u. for variable pump-probe time delay. c. tr-RIXS spectra for a selection of time delays showing a prompt melting of the CO, whereas higher energy features of the inelastic spectrum, e.g., d-d excitations/Cu^{2+} emission and charge transfer (CT) excitations, remain unaffected. Error bars represent Poisson counting uncertainties. Adapted from Ref. [81] under CC BY-NC 4.0.*

elastic) at a free-electron laser to measure the charge-order dynamics in this material after a 1.55 eV pump [81, 86]. The superlattice reflection was suppressed by up to 75% and recovered through a purely exponential relaxation, at odds with the coherent amplitude-mode oscillations observed in the Peierls systems discussed above (Fig. 6). The relaxation rate was found to be strongly momentum dependent and consistent with the presence of low-energy diffusive modes. At the lowest energies, the recovery obeys dynamic scaling laws governed by the annihilation of topological defects in the charge-order pattern. The competition between charge order and superconductivity has also been leveraged to observe the opposite effect, as quenching superconductivity with high-energy photons can enhance charge-order correlations. Wandel and co-workers demonstrated this effect in $YBa_2Cu_3O_{6+x}$ using time-resolved resonant soft x-ray scattering [87]. After an infrared pulse quenched superconductivity, the charge-order correlation length nearly doubled within roughly 1 ps in a nonthermal response. This enhancement was naturally understood as the annealing of charge-order topological defects, such as discommensurations, that are stabilized by superconductivity at equilibrium. Once the condensate is removed, the charge order becomes more coherent. In the language of Fig. 5a, removing one order deepens the free-energy minimum of the other.

Finally, optical excitation can stabilize charge-ordered states absent at equilibrium. $LaTe_3$ hosts a unidirectional charge-density wave along the c axis, while the nearly equivalent perpendicular a axis remains disordered due to a small structural anisotropy. Using ultrafast electron diffraction, Kogar *et al.* showed that photoexcitation weakens the equilibrium c-axis modulation and

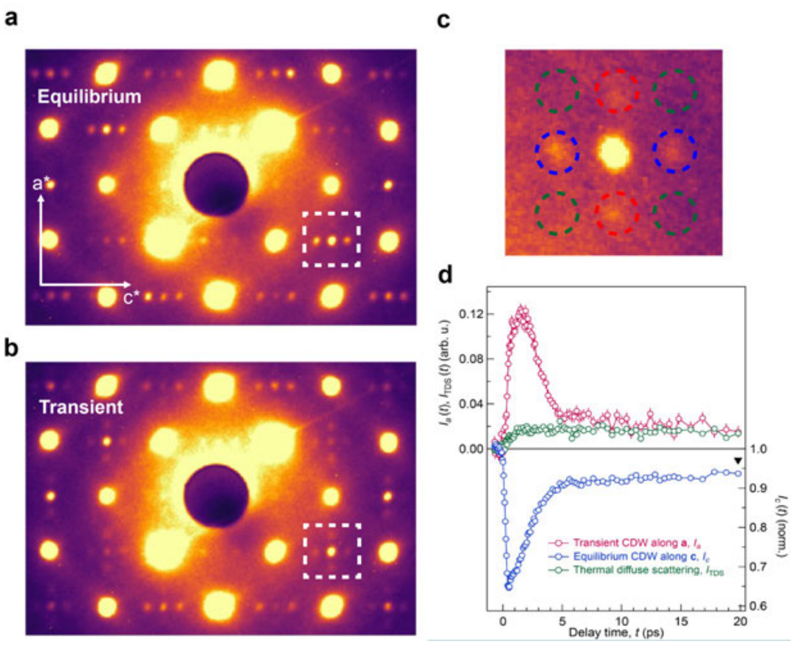

Fig. 7: *Light-induced charge-density wave in $LaTe_3$. (a)–(b) Ultrafast electron diffraction patterns before and 1.8 ps after photoexcitation with an 80 fs, 800 nm pulse. Dashed lines mark the regions where charge-order superlattice peaks appear. (c) Equilibrium c-axis satellites (blue) are suppressed while new a-axis satellites (red) emerge. Diffuse scattering is circled in green. (d) Integrated satellite intensities along the two axes as a function of time delay. The light-induced a-axis order grows as the c-axis order is quenched, and both recover on a common timescale of $\sim$1.7 ps, revealing their mutual competition. Courtesy of Dr. A. Kogar [47].*

transiently nucleates a new charge-density wave along the a axis (Fig. 7) [47]. The induced order rises within about 1 ps and decays as the original order recovers. Their nearly identical relaxation times show that the two orders draw on a common reservoir of charge carriers and are locked in direct competition. The transient a-axis wave is a genuine nonequilibrium state without counterparts in the equilibrium phase diagram, establishing light-induced excitation as a route to otherwise inaccessible states, a theme we return to in the discussion of hidden orders.

4.2 Magnetism

Magnetism is one of the most traditional arenas for the optical control of ordered states, and provides a clear example of how light-control strategies have evolved from controlling macroscopic properties (e.g., magnetization) to microscopic interactions (e.g., magnetic superexchange). Following the observation of ultrafast demagnetization in ferromagnetic nickel [88], ultrafast lasers enabled the detection and control of ferromagnetic and antiferromagnetic resonances [89,90], all-optical magnetic switching [91,92], and correlated spin dynamics across different magnetic sublattices [93]. These phenomena mostly involve changes in the macroscopic magnetization and arise from a combination of laser-induced heating, effective opto-magnetic fields, and optical perturbations of the magnetic anisotropy [20]. In this class of experiments, light acts on the spins through the electronic and optical response of the material, while the lattice enters mainly as a heat bath or passive degree of freedom.

With the advent of intense mid-infrared and THz sources, resonant protocols such as nonlinear phononics opened a new route to coherent magnetic control. In this case, coherently driven phonons, rather than photoexcited electrons, act on the spins, and the key nonlinearity is the coupling between the lattice and magnetic order, as summarized in Table 1. The lattice excitation strategy depends on the material, and rare-earth orthoferrites RFeO$_3$ have served as a model platform for these experiments. As canted antiferromagnets, their Dzyaloshinskii–Moriya interaction produces a small, magneto-optically readable net moment, while their proximity to anisotropy-driven spin-reorientation transitions amplifies weak perturbations of both THz spin resonances and rare-earth–iron f-d exchange. Magnetic states are often read out with time-resolved polarization rotation or birefringence measurements or with x-ray measurements.

In DyFeO$_3$, resonant excitation of an infrared-active B_u phonon transiently renormalizes the magnetic superexchange due to a rectified distortion along an A_g mode coordinate and coherently steers the spin-reorientation transition, demonstrating direct control of the interaction J, rather than of the magnetization alone [94]. In ErFeO$_3$, driving two near-degenerate B_u phonons with a controlled relative phase generates circular ionic motion, which mimics an effective magnetic field along the rotation axis and launches coherent spin precession [95]. Together with other experiments beyond the scope of this review, these results helped establish the field of *magnetophononics*, where lattice anharmonicity provides a symmetry-selective handle on magnetic interactions, and motivated theoretical descriptions of the effective fields, orbital moments, and exchange modulations carried by driven phonons [96, 97]. In rare-earth halides, recent theoretical [98] and experimental [99] work has shown that coherent chiral phonons, driven by circularly polarized terahertz pulses, can polarize the paramagnetic spins of cerium fluoride in a manner analogous to a quasi-static magnetic field of order 1 T. In CoF$_2$, three-phonon mixing processes of the form $Q_{IR,1}Q_{IR,2}Q_R$ distort the crystal field and decompensate the two spin sublattices, polarizing the antiferromagnet like a static piezomagnetic strain, but without changing the volume, and generating a ferrimagnetic moment of $0.2\ \mu_B$ per unit cell [100].

More recent advances have pushed these ideas from transient modulation toward magnetic states that outlive the coherent drive, connecting magnetophononics to the broader theme of light-induced metastable order. In the titanate YTiO$_3$, a ferromagnet whose order is suppressed by orbital fluctuations, Disa *et al.* showed that resonant excitation of a 9 THz oxygen rotation mode with B_{2u} symmetry enhances and stabilizes ferromagnetism, saturating the moment at low temperature and shifting the onset of order from $T_c = 27$ K to above 80 K [101]. Here, the driven phonon does not simply perturb the magnetization, but creates a more ordered state, the magnetic analog of the light-induced orders discussed for charge degrees of freedom. Such states can also be remarkably long lived. In the van der Waals antiferromagnet FePS$_3$, THz pulses tuned to a phonon and a magnon induce a metastable magnetization that persists for more than two milliseconds, with a robustness that increases as the Néel transition is approached and order-parameter fluctuations diverge [102]. In this case, proximity to criticality, rather than a structural or thermal bottleneck, stabilizes the state, a mechanism we will encounter again when discussing hidden and metastable orders.

4.3 Ferroic orders

Ferroic orders form another broad class of ordered states with fundamental and technological relevance, and light provides an effective tuning knob for many of them. Although many types of ferroic order exist, here we focus on three classes: ferroelectrics, multiferroics, and ferroaxial systems [57]. A *ferroelectric* is a material with a nonzero electric polarization that can be switched between equivalent directions by an applied electric field. A *multiferroic* hosts two or more ferroic orders, most commonly ferroelectricity and magnetism, coupled through the magnetoelectric interaction, which enables electric-field control of magnetism. Finally, *ferroaxial* systems are characterized by a rotational texture that can host vortices of electric dipoles. Ferroaxial order breaks neither spatial inversion nor time-reversal symmetry, and is considered a promising platform for nonvolatile data storage.

Some of the most compelling examples of optical control of ferroelectrics build directly on nonlinear phononics. In $LiNbO_3$, Mankowsky *et al.* demonstrated transient reversal of the ferroelectric polarization not by driving the soft polar mode directly, but by resonantly exciting a high-frequency auxiliary phonon that, through anharmonic coupling, displaces the ions along the polar coordinate [103]. The reversal could be induced in both directions, a prerequisite for switching, but remained short lived because depolarizing fields rapidly restored the original state after the drive. Overcoming this volatility requires a host whose polar order is intrinsically close to an instability, and $SrTiO_3$ is a paradigmatic example of such a system. Although its physics is rich and largely beyond the scope of this chapter, $SrTiO_3$ is a *quantum paraelectric* and lies on the disordered side of a quantum phase transition between paraelectric and ferroelectric states (Fig. 8a), where zero-point fluctuations of the polar mode suppress long-range order down to zero temperature. This proximity to a quantum critical point makes the polar order exceptionally susceptible to external perturbations.

Ultrafast experiments exploited this susceptibility directly. Nova *et al.* used mid-infrared pulses to drive the lattice of $SrTiO_3$ and reported an emergent *metastable* ferroelectric state, identified by an optical second-harmonic signal that indicates broken inversion symmetry and builds up over many pump cycles [25]. The likely mechanism behind these observations is a rectified, long-lived strain generated by the nonlinear drive, which biases the soft mode toward the polar minimum and is stabilized by the softness of the lattice near the transition. In parallel, Li and coworkers used an intense THz field tuned to the soft mode itself to drive the ions directly toward their ferroelectric positions, inducing a transient hidden ferroelectric phase [105]. Together, these indirect nonlinear phononic and direct soft-mode routes established $SrTiO_3$ as a testbed for light-induced ferroelectricity.

Disentangling the structural origin of these states requires structural probes such as time-resolved x-ray scattering. Using femtosecond x-ray diffuse scattering, Fechner *et al.* showed that resonant excitation of the 17 THz Ti–O stretching mode quenches lattice fluctuations and tips the balance between the polar instability and the competing antiferrodistortive oxygen rotations that frustrate ferroelectricity in equilibrium [106]. This picture was later refined by measurements resolving how the drive dynamically suppresses these rotations [107]. A complementary ques-

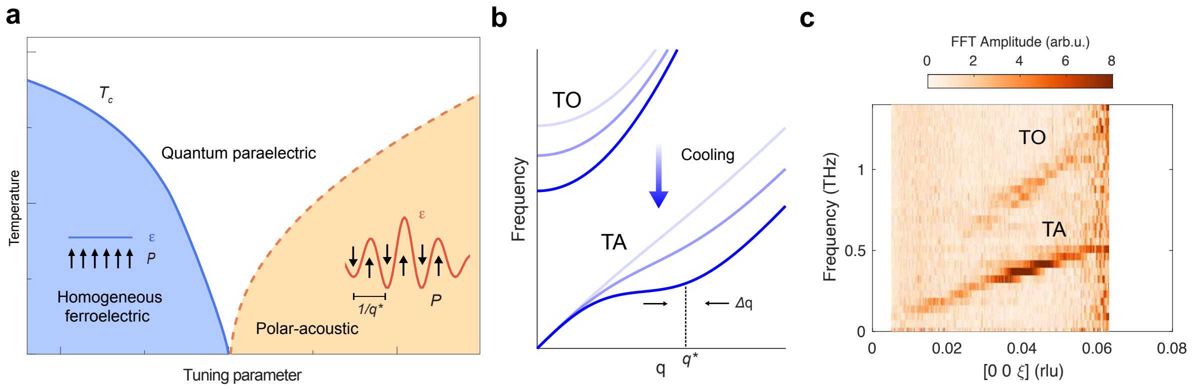

Fig. 8: *Phase diagram and low-energy modes of $SrTiO_3$. **a.** Phase diagram showing the nearby ferroelectric (blue) and polar acoustic (orange) phases around the quantum paraelectric regime. The tuning parameter here is the flexoelectric coupling strength. **b.** Dispersion of transverse phonon modes. When lowering temperature, the TO branch softens and the TA branch deviates from linear dispersion developing a kink at finite wavevector k^*, indicative of an instability. These excitations are polar and modulate the polarization spatially with a wavelength $\sim 2\pi/k^*$. **c.** Magnitude of the Fourier transform of time-domain x-ray scattering data at 20 K. Adapted with permission from Ref. [104]. Copyright (2025) by Springer Nature Limited.*

tion is whether the "failed" ferroelectric transition in $SrTiO_3$ is frustrated only by fluctuations of the uniform soft mode, or also by polar correlations at finite wavevector. To address this, Orenstein *et al.* combined single-cycle THz excitation, resonant with the soft modes of $SrTiO_3$, with femtosecond hard x-ray diffuse scattering around the $(3, 3, 3)$ Bragg peak [104]. A crucial element of this experiment was the ability to reverse the polarity of the THz field. The diffuse scattering signal at finite momentum reversed with the field, demonstrating that the observed acoustic-like oscillations carried polar character and therefore broke local inversion symmetry. Fourier-transform inelastic x-ray scattering then reconstructed the dispersion and spatial texture of these modes (Fig. 8b-c), revealing nanometer-scale *polarization density waves*, namely mesoscopic modulations of the polarization that intensify near the quantum critical point. These experiments underscore the power of x-rays to make the structural degrees of freedom underlying the ferroelectric transition directly observable.

Ultrafast experiments on multiferroics are extensive, and we use here one representative example of light control. In the spin-spiral multiferroic $TbMnO_3$, magnetoelectric coupling produces *electromagnons*, spin excitations that are active to the electric field of light rather than only to its magnetic field. Below 27 K, $TbMnO_3$ develops an incommensurate cycloidal spin order that also generates a ferroelectric polarization, making it a natural platform to test whether an optical electric field can act directly on magnetic order. Kubacka *et al.* drove the strongest electromagnon with an intense few-cycle THz pulse centered at 1.8 THz, with the electric field oriented along the crystallographic direction that activates this mode [108]. They then followed the magnetic response using femtosecond resonant soft x-ray diffraction at the Mn L_2 edge, measuring the intensity of the $(0, q, 0)$ cycloidal magnetic reflection. The diffracted intensity oscillated at the electromagnon frequency, reversed sign when the THz electric field was inverted, and was strongly suppressed outside the multiferroic phase. These observations showed that the electric-field channel opened by magnetoelectric coupling can coherently rotate the spin cycloid, providing a route to magnetic control on sub-picosecond timescales.

Recent experiments extend these control protocols to ferroaxial order. In ferroaxial systems, the order parameter is an axial vector associated with a rotational distortion, so switched domains need not be driven back by a restoring stray field. In $RbFe(MoO_4)_2$, Zeng *et al.* engineered the conjugate field to this axial order using circularly polarized THz pulses resonant with a doubly degenerate infrared-active phonon [109]. The driven phonon displacement and the THz electric field rotate together, and their cross product acts as an effective axial field whose sign is set by the light helicity. Probed by circular-dichroic second-harmonic generation, a single pulse switched the ferroaxial domain, while a pulse of opposite helicity switched it back. Remarkably, the switched state persisted for many hours, demonstrating photoinduced, nonvolatile, and rewritable ferroaxial switching.

5 Floquet engineering

We now turn to a conceptually distinct regime, in which the optical field coherently *dresses* the electronic states for as long as it is present. When a nonresonant field oscillates faster than the electrons can follow, it does not primarily deposit energy, but instead renormalizes the Hamiltonian itself, shifting and reshaping bands much as the ac Stark effect splits atomic levels [110]. *Floquet engineering* provides the natural language for this physics. It recasts a time-periodic problem in terms of an effective, time-independent Hamiltonian, turning coherent optical dressing into a quasistationary band-structure problem and making light a direct handle on the electronic Hamiltonians and topology of quantum materials [111, 112].

Following Ref. [4], the essential idea is captured by a periodically driven atomic chain (Fig. 9a). Consider noninteracting spinless fermions on a one-dimensional lattice,

$$H = -t_0 \sum_n \left(c_n^\dagger c_{n+1} + \text{H.c.} \right) = \sum_k \varepsilon(k) c_k^\dagger c_k, \qquad \varepsilon(k) = -2t_0 \cos(ka), \tag{4}$$

with hopping t_0, lattice constant a, and a cosine band of width $4t_0$. A longitudinal field $E(t) = E_0 \sin(\omega t)$ enters through the Peierls substitution $t_0 \to t_h(t) = t_0 e^{ieaA(t)/\hbar}$, where $A(t) = (E_0/\omega)\cos(\omega t)$ is the vector potential. When the drive is fast compared with the electronic timescales, the rapid phase oscillations average out, giving the time-averaged hopping

$$t_{\text{eff}} = \langle t_h(t) \rangle = t_0 J_0(F), \qquad F = \frac{aeE_0}{\hbar\omega}, \tag{5}$$

where J_0 is the zeroth-order Bessel function and F is the dimensionless drive strength. Since $|J_0(F)| < 1$, the effective hopping is reduced. This process results in the emergence of *dynamical localization* [113], as the band narrows, carriers localize, and transport is fully suppressed at the zeros of J_0. Equivalently, in momentum space the field shakes the dispersion through the minimal coupling $k \to k - eA(t)/\hbar$, so that the period-averaged band is flatter than its equilibrium counterpart (Fig. 9a). In correlated systems, the same construction can renormalize

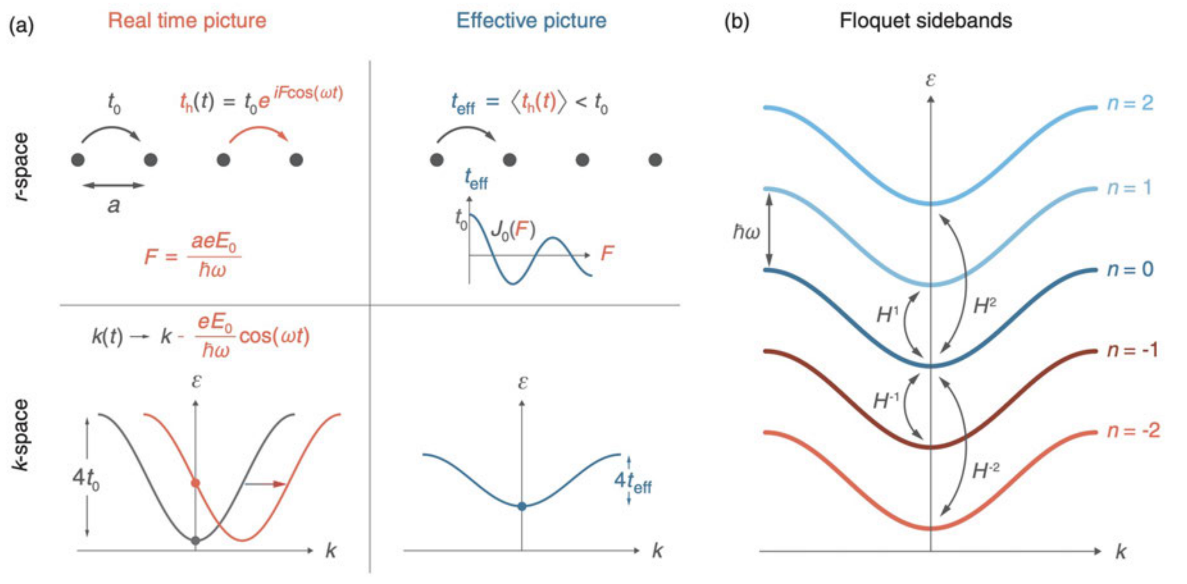

Fig. 9: *Floquet engineering of a band structure. (a) Dynamical localization in a driven atomic chain. In real time, the optical field periodically modulates the hopping and shakes the electronic band in momentum space. When time-averaged, this motion reduces the bandwidth and leads to a smaller effective hopping amplitude, $t_{\text{eff}} = t_0 J_0(F)$. (b) Floquet representation of a periodically driven system. The time-dependent Hamiltonian is mapped onto replicas of the equilibrium band structure separated by integer multiples of the drive frequency ω. Reprinted figure with permission from Ref. [4]. Copyright (2022) by the American Physical Society.*

superexchange and other electronic interactions, providing a coherent route to control strongly correlated phases [114].

This time-averaged description of coherent dressing allows the driven material to be viewed in terms of a reconstructed band structure in the presence of the electromagnetic field. For a Hamiltonian with period $T = 2\pi/\omega$, the Floquet theorem [115] allows one to write the solutions of the Schrödinger equation as $|\Psi_l(t)\rangle = e^{-i\varepsilon_l t/\hbar}|\Phi_l(t)\rangle$, where $|\Phi_l(t)\rangle$ are T-periodic states and ε_l are quasienergies, the temporal analog of crystal momentum in Bloch's theorem. Expanding the Hamiltonian in Fourier harmonics, $H_n = (1/T)\int_0^T dt\, e^{in\omega t} H(t)$, maps the time-dependent problem onto a static eigenvalue problem in an extended space

$$\mathcal{H} = \begin{pmatrix} \ddots & \vdots & \vdots & \vdots & \\ \cdots & H_0+\hbar\omega & H_{-1} & H_{-2} & \cdots \\ \cdots & H_1 & H_0 & H_{-1} & \cdots \\ \cdots & H_2 & H_1 & H_0-\hbar\omega & \cdots \\ & \vdots & \vdots & \vdots & \ddots \end{pmatrix}, \tag{6}$$

given by an infinite ladder of replicas of the time-averaged Hamiltonian H_0, H_1, H_2, shifted by integer multiples of $\hbar\omega$ and coupled by harmonics of the drive. In a solid, these replicas form *Floquet-Bloch bands*, periodic in both momentum and energy and separated by the photon energy $\hbar\omega$ (Fig. 9b). In the high-frequency limit, only H_0 remains and one recovers the dressed band of Eq. (5). At finite frequency, however, the sidebands hybridize. The higher-order terms, to leading order $H_{\text{eff}} \simeq H_0 + [H_{-1}, H_1]/\hbar\omega$ [116], open gaps and can imprint properties with no equilibrium analog, including nontrivial band topology [117–119].

Applying this elegant picture to ultrafast solid-state spectroscopy is demanding. Reaching $F \sim 1$ requires large fields, typically 10^7–10^8 Vm^{-1}, which confines experiments to short, low-frequency pulses and places coherent dressing in direct competition with heating and decoherence. Nevertheless, over the past decade, experimental advances have enabled the observation of Floquet states in a range of solid-state platforms, which we review below.

5.1 Control of band structure and functional responses

The observation of Floquet-engineered states in solids has been driven by a set of theoretical predictions. As an example, Oka and Aoki predicted that a circularly polarized field could open a gap at the Dirac point and induce a photoinduced dc Hall current [117], while Lindner, Refael, and Galitski showed that periodic driving could turn a trivial semiconductor quantum well into a *Floquet topological insulator* hosting helical edge states [118]. These proposals established that optical fields could be used to actively manipulate the band topology.

Resolving coherent band-structure dressing requires a momentum-resolved probe, and trARPES quickly became the technique of choice for these experiments. In a landmark work, Wang *et al.* excited the topological surface states of Bi_2Se_3 with mid-infrared pulses (≈120 meV) and used trARPES to image the emergence of Floquet-Bloch replicas of the Dirac cone [34]. These replicas only appeared upon hybridization between the light-field and the electrons at overlap with the pump and were separated by the photon energy, as discussed in the previous section. Further, they developed gaps at crossing points between bands of different Floquet order, thus providing direct evidence that light could coherently reconstruct the band structures.

The interpretation of these spectra, however, requires some care, as addressed in subsequent work by Mahmood *et al.* [35]. Floquet-Bloch states are dressed states of the *Bloch electrons inside the crystal*, as they inherit the properties of the equilibrium bands of a material and disperse as replicas of those bands. Volkov states, by contrast, are dressed states of the *outgoing photoelectron in vacuum*. They are also referred to as laser-assisted photoemission (LAPE), and their sidebands are tied to the free-electron final state rather than to the band structure of the material. Since both effects generate replicas spaced by $\hbar\omega$, and since the two channels can interfere at the surface, distinguishing them is essential. This can be achieved by eliminating the out-of-plane electric field of the pump. By tuning the pump polarization and exploiting the different momentum dependence of the two couplings, Mahmood *et al.* showed that the Volkov contribution can be suppressed, allowing the genuine Floquet-Bloch response to be isolated.

How rapidly this dressing is established was addressed by Ito *et al.*, who used subcycle trARPES to follow the topological surface state of Bi_2Te_3 under a strong, phase-stable mid-infrared drive [36]. The pump was an in-plane, s-polarized field centered at 25 THz ($\hbar\Omega \simeq 0.1$ eV), with a surface field of ~ 0.8 $\text{MV}\,\text{cm}^{-1}$, while the probe was a 17 fs ultraviolet beam. They first observed a pump-induced intraband current that appeared as an asymmetry of the Dirac cone, roughly one half-cycle before the field maximum. Then, Floquet-Bloch sidebands emerged within a single optical cycle and gained strong weight near the field crest. Thus, in a sufficiently coherent band, Floquet dressing can form on the timescale of one optical period, linking band-structure engineering directly to the intraband acceleration and interband transitions in solids. Floquet dressing was demonstrated at nearly the same time in a semiconductor, where Zhou *et al.* hybridized the valence band of black phosphorus with the $n = -1$ replica of the conduction band, opening a dynamical gap that decayed within ~ 130 fs [120].

Graphene, the system for which Floquet topological gaps were first predicted, has also been driven into Floquet-engineered states with mid-infrared light. In a picosecond transport experiment, McIver *et al.* drove monolayer graphene with circularly polarized mid-infrared pulses (46 THz, 191 meV) and sampled the transverse current on-chip with a laser-triggered photoconductive switch, observing a light-induced anomalous Hall effect [53]. The gate dependence revealed a ~ 60 meV conductance plateau around the Dirac point, where a Haldane-like Floquet gap is expected, with an anomalous Hall conductance approaching $1.8\, e^2/h$. Direct spectroscopic evidence arrived only recently, because graphene poses additional constraints for trARPES experiments: its Dirac cone lies at the K point, requiring high-harmonic probe photons, while Volkov sidebands and fast scattering can obscure weak Floquet replicas. Two back-to-back recent trARPES studies overcame these obstacles and successfully reported evidence for Floquet replicas in graphene (Fig. 10). Choi *et al.* used a 5 μm (246 meV) mid-infrared drive and a 26.4 eV probe to resolve replica Dirac cones in monolayer epitaxial graphene. By rotating the pump polarization, they showed that the replicas arise from the scattering between Floquet-Bloch and Volkov states [121]. Merboldt *et al.* reached the same conclusion with time-resolved momentum microscopy, using a 0.65 eV infrared drive and a 26.5 eV extreme-ultraviolet probe. The momentum asymmetry of the sidebands, together with calculations including ultrafast dephasing, showed that Floquet sidebands survive even when scattering broadens the light-induced gaps [122]. Similar experiments have also yielded Floquet-engineered states and gap opening beyond Dirac semimetals. Bielinski *et al.* used helicity-dependent, circularly polarized mid-infrared driving and trARPES to control the Dirac mass gap of the topological antiferromagnet $MnBi_2Te_4$, with opposite pump helicities producing different gaps [37].

Because Floquet engineering reshapes electronic structure, it also appears in optical and functional responses. A clear example is that of valleytronics in monolayer transition-metal dichalcogenides. Sie *et al.* used intense circularly polarized light tuned below the gap of monolayer WS_2 and transient exciton reflectance to resolve a valley-selective *optical (ac) Stark shift* up to 18 meV [123], and later isolated the much smaller *Bloch-Siegert shift* [124]. Valley-selective circular dichroism was key to separate the two contributions, providing a textbook example of Floquet dressing in an effective two-level system. These experiments showed that the co-rotating field component produces the optical Stark shift, whereas the usually neglected counter-rotating component produces the Bloch-Siegert shift.

The examples discussed so far largely involve weakly interacting band electrons. A complementary limit appears when the field dresses localized single-ion multiplets. Shan *et al.* drove the magnetic insulator $MnPS_3$ far off resonance from the on-site Mn d-d transition, using fields

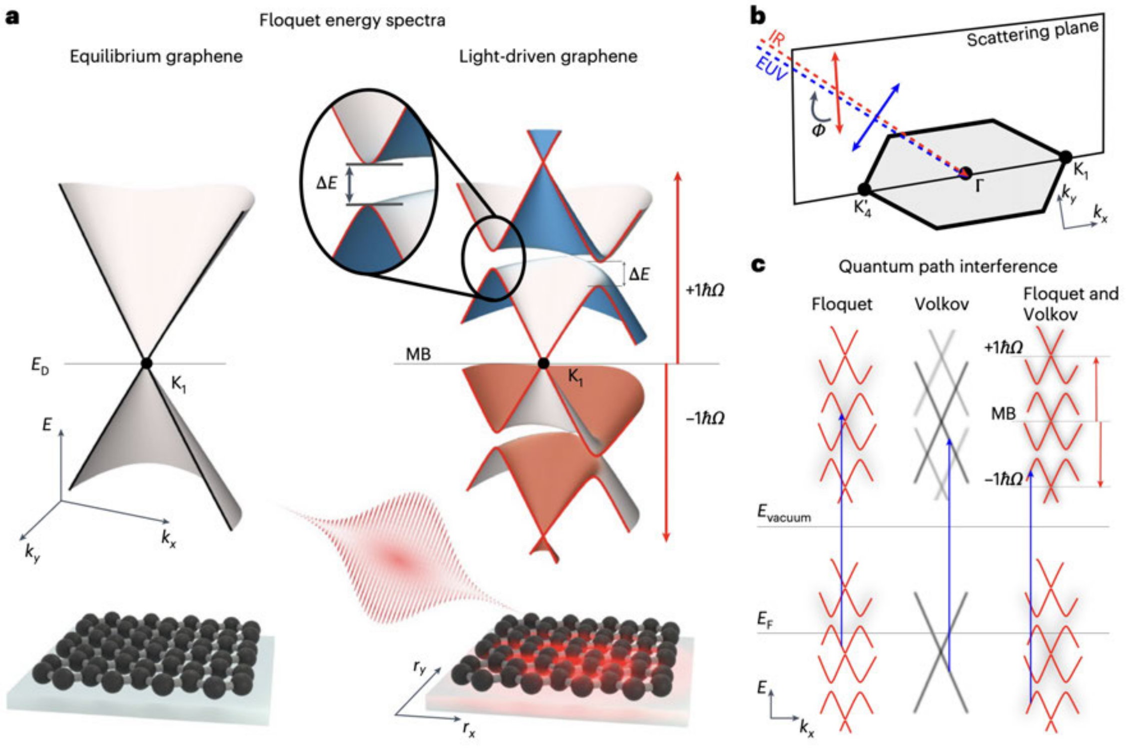

Fig. 10: *Floquet engineering of electronic bands in graphene. (a) Energy- and in-plane-momentum-resolved sketch of the graphene bands near the K point in equilibrium (black) and under periodic driving (red). Coherent dressing produces sidebands of the main Dirac band, spaced by the drive photon energy $\hbar\Omega$, and energy gaps ΔE that open where sidebands of different photon order cross and hybridize. (b) Experimental geometry of the pump probe experiment. (c) Resulting Floquet and Volkov states, as well as their quantum interference. Reprinted from Ref. [122], licensed under a Creative Commons Attribution 4.0 International License. Copyright (2025) by the authors.*

of order 10^9 Vm^{-1}, and observed coherent on-off switching of the second-harmonic efficiency within 100 fs, with an on-off ratio exceeding ten and no measurable dissipation [125]. This response corresponds to a giant Floquet renormalization of the optical nonlinearity. In a different experiment, Zhang *et al.* used off-resonant linearly polarized light and time-resolved second-harmonic generation to induce an electronic polarization in antiferromagnetic Cr_2O_3 [26]. These studies broaden Floquet engineering from the reshaping of itinerant bands to the control of atomic-like states and single-ion responses.

5.2 Towards quantum control of correlated states

When periodic driving addresses only a few isolated electronic levels, Floquet engineering becomes a form of quantum control. This limit has a long history in weakly interacting systems, where ultrafast optical fields have produced coherent Rabi rotations, picosecond population control, and complete state manipulation in atoms, semiconductor excitons, and quantum dots [126–129]. Extending this control to strongly correlated electrons is a central frontier [4,5], both because these systems host the most dramatic nonequilibrium responses and because periodic driving is predicted to renormalize interactions and stabilize exotic electronic phases. The key challenge is to identify correlated states that can be coherently addressed and read out before dissipation and decoherence destroy the coherent Floquet dressing.

Hubbard excitons in one-dimensional Mott insulators are a compelling platform for demonstrating Floquet engineering of many-body states. Unlike conventional electron-hole excitons, they are bound holon-doublon pairs stabilized by Coulomb repulsion [130, 131]. Together with spin-charge separation, this binding leads to nearly degenerate even- and odd-parity states. They therefore realize a many-body, two-level system with strong, well-characterized linear and nonlinear optical responses [132, 133]. Their few-level structure gives direct access to the coherent evolution of the many-body wavefunction, which is otherwise difficult to isolate from band renormalization and symmetry breaking in more complex correlated materials.

Driving the excitons with an intense, nonresonant mid-infrared field $\vec{E}_{\mathrm{MIR}}(t) = \vec{E}^0_{\mathrm{MIR}} \cos(\Omega t)$ couples the bright odd state $|u\rangle$ and the dark even state $|g\rangle$ through $\hat{H}_{\mathrm{int}}(t) = \vec{\mu}_{ug} \cdot \vec{E}_{\mathrm{MIR}} \, |u\rangle\langle g| + \mathrm{h.c.}$ The optical Stark and Bloch-Siegert shifts, the usual fingerprints of Floquet driving, carry opposite signs and nearly cancel for a degenerate pair [123–125], so that the dominant effect is a coherent mixing of the two parities within the optical cycle. The Floquet states retain their quasienergy but acquire a time-dependent composition,

$$|u(t)\rangle = e^{iE_{\mathrm{exc}}t/\hbar} \left[\cos \tfrac{\vartheta(t)}{2} |u\rangle + \; e^{i\varphi(t)} \; \sin \tfrac{\vartheta(t)}{2} |g\rangle \right] \tag{7}$$

$$|g(t)\rangle = e^{iE_{\mathrm{exc}}t/\hbar} \left[\cos \tfrac{\vartheta(t)}{2} |g\rangle - e^{-i\varphi(t)} \sin \tfrac{\vartheta(t)}{2} |u\rangle \right] \tag{8}$$

which describes a coherent rotation of the many-body wavefunction on a Bloch sphere spanned by the even and odd excitons, with polar and azimuthal angles $\vartheta(t)$ and $\varphi(t)$ evolving at twice the drive frequency. Cycle-averaged, this rotation redistributes spectral weight into Floquet sidebands at $E_{\mathrm{exc}} \pm 2n\Omega$ for $|u(t)\rangle$ and $E_{\mathrm{exc}} \pm (2n{+}1)\Omega$ for $|g(t)\rangle$. Although the drive is far off-resonance, at strong fields the coupling $g = \vec{\mu}_{ug} \cdot \vec{E}_{\mathrm{MIR}}$ becomes comparable to Ω, so the Rabi frequency locks to the drive frequency and g sets only the amplitude of the rotation. This ultrastrong-coupling regime, made possible jointly by the near-degeneracy of the excitons and the large field, departs from conventional resonant two-level driving and from the quantum-dot experiments above, where the coupling is smaller than both level splitting and drive frequency.

Baykusheva *et al.* implemented this protocol in the chain cuprate Sr_2CuO_3 [134]. Here, Hubbard excitons form two near-degenerate levels around 1.72 eV. A mid-infrared pump at 0.12 eV (28 THz), far below the 1.8 eV Mott gap, dresses the exciton, while a near-infrared probe generates resonant third-harmonic emission at the exciton energy. Because $|g\rangle$ is dark, rotation toward the even state suppresses the third-harmonic yield by up to 70% at 1.8 MV cm^{-1} (Fig. 11). The polarization and field dependences follow the J_0 Bessel form expected for Floquet dressing, and probe detuning reveals a genuine sub-gap Floquet sideband in $\chi^{(3)}$, showing that coherence survives several drive cycles. At higher fields, the wavefunction undergoes continuous oscillatory rotations, reaching an instantaneous angle of $\pi/2$ at 1.7 MV cm^{-1}. This uniaxial $\pi/2$ rotation is the minimal building block of programmable quantum control sequences based on pulse shaping techniques and opens the route to Ramsey interferometry, dynamical decoupling, and ultimately full SU(2) control of correlated many-body wavefunctions [135–137].

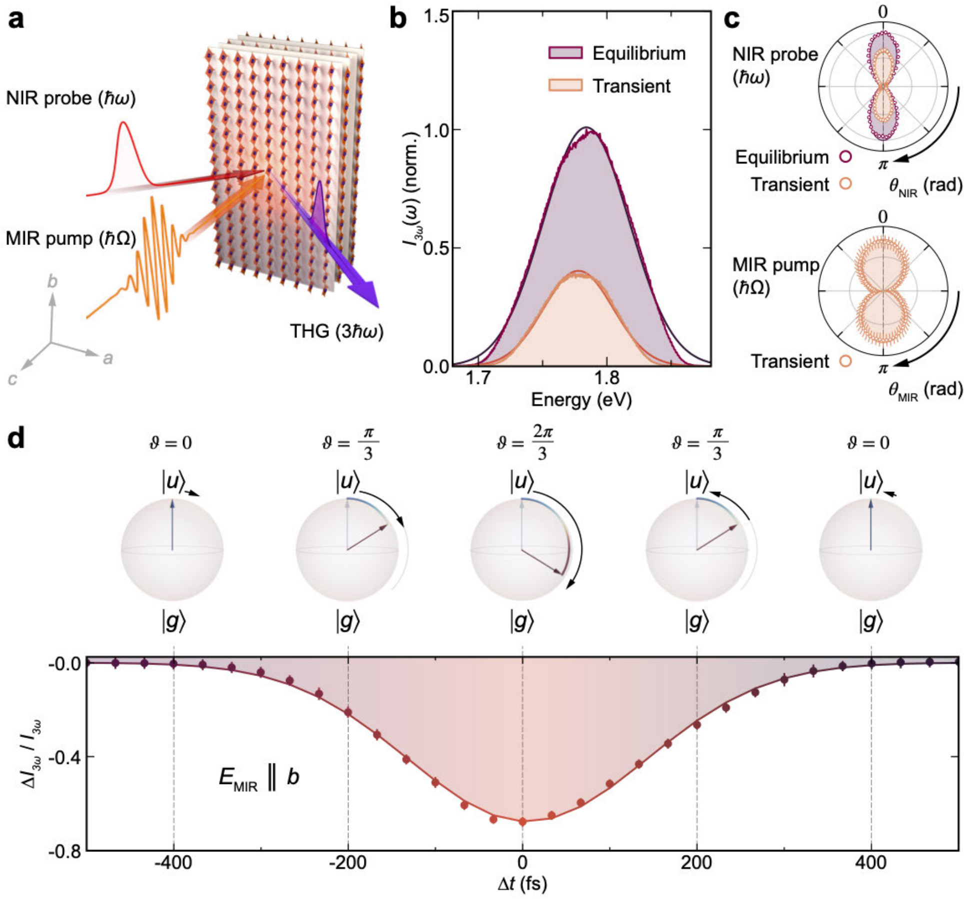

Fig. 11: *Quantum control of Hubbard excitons in* Sr_2CuO_3*. (a) Sketch of the mid-infrared pump (*$\hbar\Omega = 0.12$ *eV) third-harmonic emission (THG) probe experiment. (b) Normalized THG spectra of a 0.59 eV probe at equilibrium (purple) and at zero delay after a 1.8 MV* cm^{-1} *pump (orange). (c) THG intensity as a function of probe (top) and pump (bottom) polarization angle. The suppression vanishes for a pump polarized normal to the chains and follows the* $1 - J_0(A_1 \cos\theta)^4$ *dependence (solid line) expected for Floquet dressing. (d) Time-resolved differential THG* $\Delta I_{3\omega}/I_{3\omega}$ *for* $E_{\mathrm{MIR}} = 1.8$ *MV* cm^{-1}*. The Bloch spheres mark the instantaneous rotation angle* ϑ *at selected delays. Reprinted with permission from Ref. [134]. Copyright (2026) by Springer Nature Limited.*

5.3 Electronic metastability via coherent dressing

The Floquet-engineered states discussed so far exist only while the drive is present. Because the dressed bands and gaps arise from hybridization with the photon field, they decay once pump coherence dissipates, and the renormalized Hamiltonian returns to its equilibrium form. This short lifetime is the main obstacle to converting Floquet-engineered states into persistent, functional states of matter. One alternative route is to use longer drives, but this requires careful control of energy dissipation to avoid runaway heating. Another is to use dressing not as an end in itself, but as a transient *gate*. While present, the field can lift a symmetry that otherwise forbids a quantum process, allowing the system to cross a barrier into a configuration that survives after the drive is gone. Once the symmetry is restored, the reverse pathway is again blocked, leaving the system trapped in a long-lived metastable state.

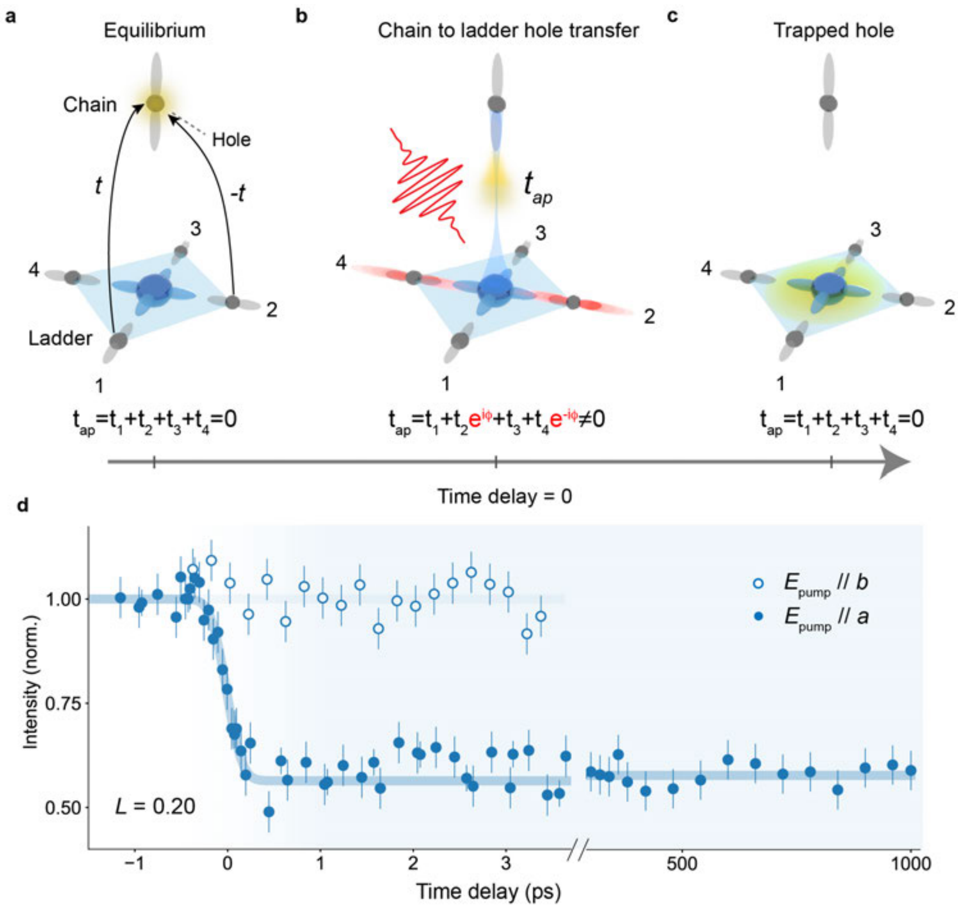

Fig. 12: *Electronic metastability in $Sr_{14}Cu_{24}O_{41}$. **a.** Each plaquette on the ladder features O 2p (grey) and Cu 3d (blue) orbitals constituting a Zhang-Rice singlet. At equilibrium, holes mostly reside on the chains and the approximate D_{4h} symmetry makes the hopping contributions to the apical chain oxygen alternate in sign and cancel, resulting in vanishing hopping t_{ap} between chains and ladders. **b.** However, this symmetry is broken when the Hamiltonian is dressed by an intense in-plane pump field E_{pump} (time delay = 0), resulting in a nonzero t_{ap}. The transient activation of the symmetry-forbidden hopping t_{ap} leads to a chain-to-ladder hole transfer. **c.** Once the field is removed, t_{ap} vanishes, trapping the transferred holes in the ladder. **d.** Time-dependent charge-order diffraction intensity at $L = 0.20$. For an in-plane pump ($E_{\mathrm{pump}} \parallel a$, filled circles) the charge order is suppressed within the pulse and remains so up to nanosecond delays, whereas an out-of-plane pump ($E_{\mathrm{pump}} \parallel b$, open circles) produces no suppression, as expected for the symmetry-activated mechanism. Adapted with permission from Ref. [49]. Copyright (2025) by Springer Nature Limited.*

A recent realization of this idea was demonstrated in the optically driven cuprate ladder [49]. The cuprate material $Sr_{14}Cu_{24}O_{41}$ is a self-doped charge-transfer insulator consisting of two nearly decoupled subsystems: hole-rich chains that act as charge reservoirs, and two-leg ladders that host charge order below 250 K. Padma *et al.* excited single crystals with intense near-infrared pulses (1.55 eV, just below the charge-transfer gap, up to 7.7 MV cm^{-1}) polarized in the ladder plane, and tracked the response with time-resolved THz reflectivity, trXRD, trXAS, and trRIXS. From the charge-ordered state, the 100-fs pump induces a nonequilibrium

electronic state that persists for tens of nanoseconds, far beyond the pulse duration (Fig. 12**d**). trXAS reveals a transfer of roughly 3% holes per Cu from chains to ladders, trXRD shows the concomitant suppression of charge-order correlations, and the low-energy response develops emergent collective modes [138]. Together, these probes identify a metastable state stabilized by the transient activation of an otherwise forbidden chain-to-ladder hopping channel.
Why this channel is closed at equilibrium, and how light opens it, follows from a transparent symmetry argument (Fig. 12**a-c**). The doped holes in the ladder occupy Zhang-Rice singlets built from the Cu $3d_{x^2-y^2}$ orbital and the surrounding in-plane O $2p$ orbitals. The relevant ligand combination is the symmetric superposition

$$\psi_p(\mathbf{r};\mathbf{R}) = \frac{1}{2}\Big[\psi_{p_x}(\mathbf{r};\mathbf{R}-\tfrac{a_0}{2}\hat{x}) - \psi_{p_x}(\mathbf{r};\mathbf{R}+\tfrac{a_0}{2}\hat{x}) + \psi_{p_y}(\mathbf{r};\mathbf{R}-\tfrac{a_0}{2}\hat{y}) - \psi_{p_y}(\mathbf{r};\mathbf{R}+\tfrac{a_0}{2}\hat{y})\Big], \quad (9)$$

which, like the $3d_{x^2-y^2}$ orbital it accompanies, is antisymmetric under a quarter rotation about the Cu–apical-oxygen axis,

$$\hat{R}\big(\tfrac{\pi}{2}\big)\,\psi_p(\mathbf{r};\mathbf{R}) = -\psi_p(\mathbf{r};\mathbf{R}), \quad (10)$$

whereas the apical-oxygen $2p_z$ orbital that bridges the ladder to the chain is invariant under this symmetry operation. The hopping integral between the ladder state and the apical oxygen is then a sum of four rotated contributions whose alternating signs cancel exactly,

$$t_{ppz} = \frac{1}{4}\left[\int \psi^*_{2p_z}\,\mathcal{H}\,\psi_p\,d\mathbf{r}^3 - \int \psi^*_{2p_z}\,\mathcal{H}\,\psi_p\,d\mathbf{r}^3 + \int \psi^*_{2p_z}\,\mathcal{H}\,\psi_p\,d\mathbf{r}^3 - \int \psi^*_{2p_z}\,\mathcal{H}\,\psi_p\,d\mathbf{r}^3\right] = 0, \quad (11)$$

so the chains and ladders are decoupled by symmetry. An intense in-plane field can lift this symmetry and produce a transient tunneling matrix element. Introducing the field through the minimal coupling

$$\mathcal{H}(\mathbf{A}) = \mathcal{H}(\mathbf{A}{=}0) - \frac{e}{2m_e c}\sum_j \big[i\hbar\nabla_j \cdot \mathbf{A}(\mathbf{r}_j) + \text{h.c.}\big] + O(\mathbf{A}^2), \quad (12)$$

and incorporating it as a Peierls phase on the hopping, $t(\mathbf{r}_i,\mathbf{r}_j)\to t(\mathbf{r}_i,\mathbf{r}_j)\exp\big(\frac{ie}{\hbar c}\int_{\mathbf{r}_i}^{\mathbf{r}_j}\mathbf{A}(\mathbf{r})\cdot d\mathbf{r}\big)$, unbalances the four contributions according to their orientation relative to the field. The cancellation is now incomplete, and the apical hopping becomes finite,

$$t_{ppz} = \frac{1}{2}\Big(t_{pp}+t_{pp}-t_{pp}e^{-i\frac{eA_0a_0}{2\hbar c}}-t_{pp}e^{i\frac{eA_0a_0}{2\hbar c}}\Big) = t_{pp}\left[1-\cos\Big(\frac{eA_0a_0}{2\hbar c}\Big)\right] \simeq \frac{1}{2}\Big(\frac{eA_0a_0}{2\hbar c}\Big)^2 t_{pp} \propto A_0^2, \quad (13)$$

scaling as the square of the field amplitude. Averaging over the drive period recovers the steady-state effective hopping that characterizes the coherently-dressed ladder,

$$t^{(\text{eff})}_{ppz} = \frac{\Omega}{2\pi}\int_0^{2\pi/\Omega} t_{pp}\left[1-\cos\Big(\frac{ea_0A_0\cos(\Omega\tau)}{2\hbar c}\Big)\right]d\tau = \left[1-\mathcal{J}_0\Big(\frac{ea_0A_0}{2\hbar c}\Big)\right]t_{pp}, \quad (14)$$

where $\mathcal{J}_0$ is the zeroth-order Bessel function. In the weak-field limit, this activated hopping also grows as A_0^2. It acts as a transient gate: while the pulse is present, holes flow from the chains into the lower-density ladders; once coherence is lost, symmetry is restored, $t_{ppz} \to 0$, and the transferred holes are trapped. The same symmetry argument applies to the Cu orbital matrix elements, as discussed in Ref. [49]. The observed E^2 scaling and the absence of a response for out-of-plane polarization are therefore direct fingerprints of symmetry-activated charge transfer.

Metastable photoinduced states are otherwise rare, and typically rely on material-specific cooperative effects, often involving the lattice, that trap the system behind a structural barrier. The significance of this experiment is that it isolates a purely electronic, symmetry-based route to metastability without structural transitions. Coherent optical dressing transiently switches on a forbidden term in the Hamiltonian, redistributes charge, and then leaves the system trapped once the symmetry is restored. This establishes transient Hamiltonian engineering as a general design principle for metastable quantum states, applicable wherever symmetry separates a material into weakly coupled sectors.

6 Light-induced superconductivity

As seen in the previous sections, coherent control can drive materials into ordered states. A major challenge is whether light can also engineer macroscopic quantum coherence and produce superconducting responses with enhanced or emergent properties at temperatures far above those accessible in equilibrium. This section reviews the experimental evidence for *light-induced superconductivity*, and the theoretical scenarios proposed to explain it.

6.1 Experimental reports of light-induced superconductivity

The relationship between light and superconductivity is often antagonistic. Superconducting condensates are among the most fragile electronic ground states, and eV photons have been shown to readily destroy them by breaking Cooper pairs, populating the gap with hot quasiparticles, and quenching macroscopic phase coherence. Pump–probe experiments have long exploited this effect to track the suppression and recovery of superconductivity, following pair-breaking and re-condensation dynamics in cuprates and conventional superconductors through their transient THz response [139–142].

However, light can in some cases *enhance* superconducting coherence rather than degrade it. In conventional superconductors near T_c, weak sub-gap microwave irradiation can sharpen the gap and modestly raise T_c, an effect first observed by Wyatt and Dayem and later described by Eliashberg [143–145]. This microwave-stimulated superconductivity is small, confined to a narrow window around T_c, and arises because light redistributes quasiparticles away from the gap edge near the Fermi level, enhancing the coherence of an already formed condensate. The more radical idea pursued over the past fifteen years is that intense mid-infrared driving may instead stimulate condensation far from equilibrium, starting from a normal metal and transiently producing superconducting correlations well above the equilibrium T_c.

Optical signatures of superconductivity. The optical properties of a superconductor are remarkable and provide a clear fingerprint for pump–probe experiments [146, 147]. Since pairing gaps typically lie in the meV range, the natural probe is time-resolved THz spectroscopy, which accesses these energy scales and measures the complex conductivity $\tilde{\sigma}(\omega, \Delta t) = \sigma_1(\omega, \Delta t) + i\sigma_2(\omega, \Delta t)$ as a function of pump–probe delay Δt.[1] At equilibrium, a normal metal is described by the Drude model,

$$\tilde{\sigma}(\omega) = \frac{\sigma_{\mathrm{dc}}}{1 - i\omega\tau}, \quad \text{where} \quad \sigma_1(\omega) = \frac{\sigma_{\mathrm{dc}}}{1 + \omega^2\tau^2}, \quad \text{and} \quad \sigma_2(\omega) = \frac{\sigma_{\mathrm{dc}}\,\omega\tau}{1 + \omega^2\tau^2}. \tag{15}$$

A Drude metal displays a dissipative peak in σ_1 centered at zero frequency, while the reactive part vanishes, $\sigma_2(\omega) \to 0$ as $\omega \to 0$. As the superconducting state develops, the coherent part of this Drude weight collapses into a zero-frequency δ function in the real conductivity,

$$\sigma_1(\omega) = \pi\,\frac{n_s e^2}{m}\,\delta(\omega) + \sigma_1^{\mathrm{reg}}(\omega), \tag{16}$$

where n_s is the superfluid density and the regular part σ_1^{reg} is gapped, with dissipative absorption suppressed below the pair-breaking edge 2Δ. The spectral weight removed from finite frequencies is conserved and transferred entirely to the zero-frequency δ function, as required by the Ferrell–Glover–Tinkham sum rule [147]. Through the Kramers–Kronig relations, this δ function in σ_1 enforces a purely inductive, divergent imaginary conductivity,

$$\sigma_2(\omega) = \frac{n_s e^2}{m\,\omega} = \frac{1}{\mu_0\lambda_L^2\,\omega} \;\propto\; \frac{1}{\omega}, \qquad \lambda_L = \left(\frac{m}{\mu_0 n_s e^2}\right)^{1/2}, \tag{17}$$

where λ_L is the London penetration depth. The essential point is that this $1/\omega$ inductive response follows from the condensate itself, namely from the zero-frequency δ function in σ_1, and not from the detailed gap structure. It is therefore universal and survives even for strongly anisotropic or nodal gaps, as in the d-wave cuprates, where σ_1^{reg} lacks a sharp gap edge. The experiments reviewed below search for this transient above-T_c signature in the THz response after resonant mid-infrared excitation, possibly accompanied by a gap-like suppression of σ_1.

Cuprates. Building on structural control through nonlinear phononics (Section 3.3) and on the competition between charge order and pairing (Section 4.1), the first experiment in this direction sought to enhance superconductivity by suppressing a competing order in the driven state. Fausti *et al.* studied the stripe-ordered cuprate $La_{1.675}Eu_{0.2}Sr_{0.125}CuO_4$, a $1/8$-hole-doped compound in which static charge stripes suppress bulk superconductivity [149]. Resonant excitation of an in-plane Cu–O stretching mode transiently induced an inductive response in $\sigma_2(\omega, \Delta t)$, together with a Josephson plasma edge in the c-axis reflectivity, the hallmark of three-dimensional interlayer superconducting coupling. A Josephson plasma resonance is the collective oscillation of the interlayer phase of the superconducting condensate, sustained by Cooper-pair tunneling between the CuO_2 planes. The results were interpreted as the revival of

[1] There are subtleties in interpreting the instantaneous THz conductivity as a quasi-equilibrium optical conductivity, but they go beyond the scope of these lecture notes.

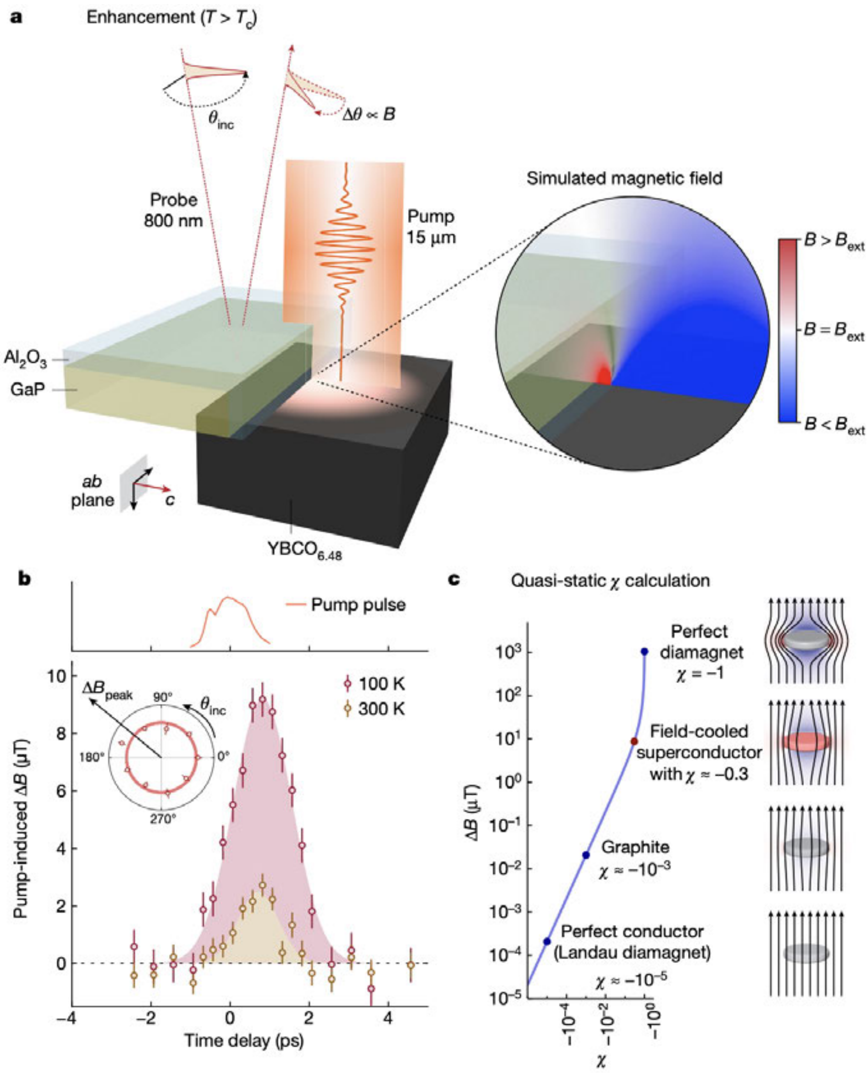

Fig. 13: *Meissner effect in an optically-driven cuprate.* ***a.*** *Transient expulsion of an applied magnetic field from optically driven $YBa_2Cu_3O_{6.48}$, measured by ultrafast Faraday-rotation magnetometry after resonant excitation of the apical-oxygen phonon.* ***b.-c.*** *The diamagnetic screening response, observed far above the equilibrium T_c, corresponds to an inferred volume susceptibility $\chi \simeq -0.3$ and constitutes a direct magnetic fingerprint of a transient superconductor. Reprinted from Ref. [148], licensed under a Creative Commons Attribution 4.0 International License. Copyright (2024) by the authors.*

latent superconducting fluctuations following pump-induced melting of the competing stripe-ordered state, in close analogy with the charge-order dynamics discussed in Section 4.1.

Following this early result, experiments then focused on bilayer cuprates $YBa_2Cu_3O_{6+x}$ (YBCO), generally regarded as cleaner and less inhomogeneous copper oxides. These materials can be idealized as a stack of inequivalent Josephson junctions. The thin *intra*-bilayer and thick *inter*-bilayer junctions produce two longitudinal Josephson plasmons, a low-frequency inter-bilayer mode near 30 cm^{-1} and a high-frequency intra-bilayer mode near 475 cm^{-1}, together with a transverse plasmon in σ_1 whose weight tracks the c-axis superfluid density. Hu *et al.* resonantly drove the apical-oxygen B_{1u} phonon at ~ 17 THz (~ 15 μm), a mode tied to a structural parameter that correlates with T_c [150], and found that light induces (1) a transient $1/\omega$ inductive response and (2) a *redistribution* of coherence between the two Josephson plasmons. The inter-bilayer mode blue-shifts and strengthens, while the intra-bilayer mode red-shifts, with the total coherent spectral weight approximately conserved [151, 152]. Notably, this enhancement persists far above T_c, up to temperatures coincident with the pseudogap line rather than with T_c, and appears even in underdoped samples with weaker charge-order correlations. These results suggest a connection to the pseudogap state and, possibly, a response of *preformed pairs* already present in the normal state. Femtosecond x-ray diffraction further constrained the accompanying lattice motion. By reconstructing the transient structure of driven YBCO from a subset of diffraction peaks, Mankowsky *et al.* identified a genuine lattice distortion induced via nonlinear-phononic coupling, but with displacements of only a picometer, or a few tenths of a percent of the relevant bond lengths [44]. Moreover, this distortion is smaller than, and opposite in sign to, the static structural difference between higher- and lower-T_c cuprates. These observations imply that structural rearrangements alone cannot explain the full enhancement of superconducting coherence, and suggest that the origin of this effect is mainly electronic.

In recent years, it has become clear that optical signatures, however suggestive, may not by themselves distinguish a genuine superconductor from a metal with anomalously high mobility. To resolve this fundamental ambiguity, it is necessary to perform ultrafast measurements of magnetic expulsion. Using ultrafast optical magnetometry, Fava *et al.* detected expulsion of an applied magnetic field from optically driven $YBa_2Cu_3O_{6.48}$, a transient Meissner effect with inferred volume susceptibility $\chi \simeq -0.3$ that persists up to room temperature [148] (Fig. 13). Because diamagnetic screening is the hallmark of a phase-coherent condensate and does not rely on model-dependent inversions of reflectivity data, this result provides the strongest evidence to date that light enhances superconducting coherence in these materials.

Fullerides. Signatures of light-enhanced superconductivity are not unique to the cuprates, and have been detected also in different families of organic metals. The most extensively characterized case is that of the alkali-doped fulleride K_3C_{60}, where the effect appears far from any obvious competing order and in a material with a more conventional equilibrium superconductivity. At equilibrium, K_3C_{60} is a superconductor ($T_c = 20$ K) with three narrow, half-filled bands derived from the C_{60} t_{1u} orbitals close to the Fermi level [153]. In this system, pairing is believed to arise from the cooperation of strong electronic correlations and coupling to intramolecular Jahn–Teller vibrations. In the simplest BCS mean-field form, the equilibrium transition temperature is given by $k_B T_c = 1.13\hbar\omega_D e^{-\frac{1}{N(\varepsilon_F)V}}$, where ω_D is the phonon Debye frequency, $N(\varepsilon_F)$ is the density of states at the Fermi level, and V is the effective pairing interaction. T_c increases with both the characteristic phonon energy and, more dramatically, with the density of states and pairing interaction. A natural question is whether nonlinear phonon excitation can be conducive to an enhanced superconducting state by modulating any of these parameters. The infrared-active T_{1u} modes can be driven directly by a mid-infrared field but do not couple, by symmetry, to the t_{1u} electrons. The pairing modes are instead the Raman-

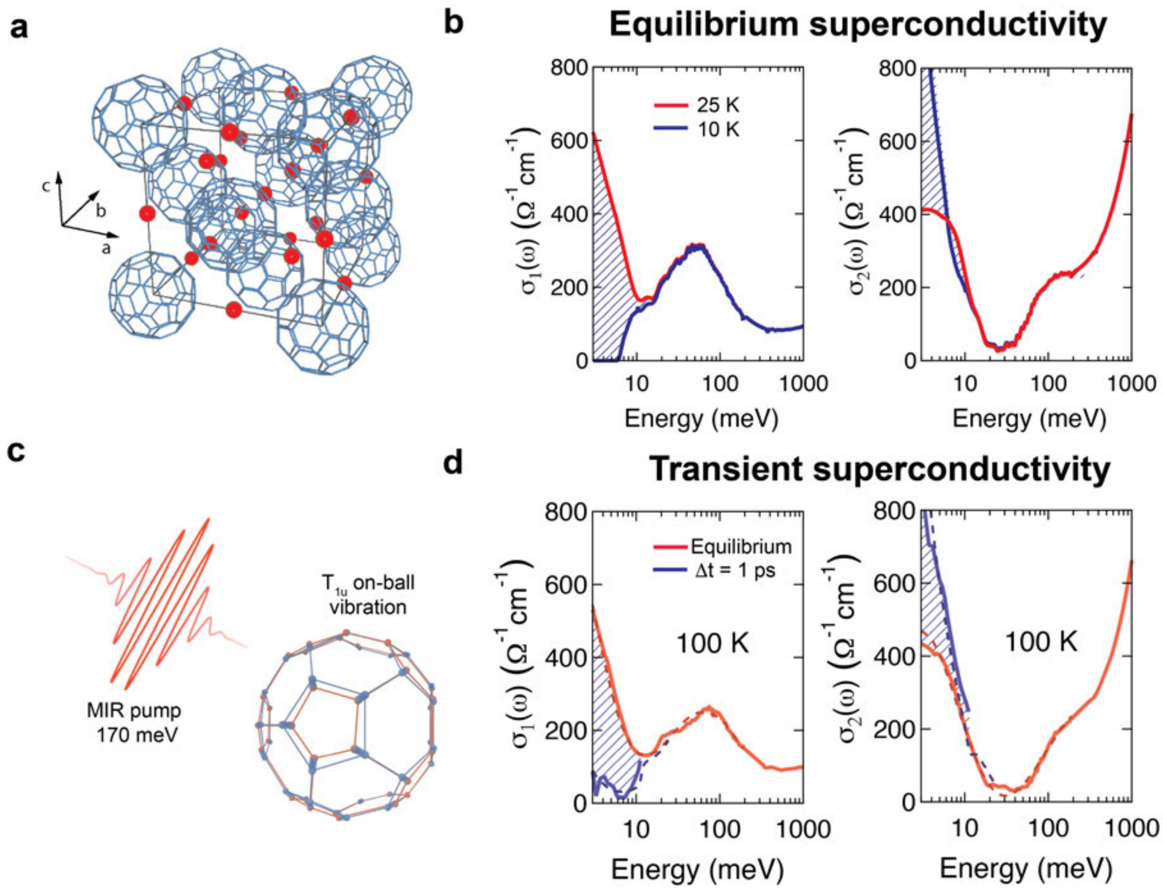

Fig. 14: *Light-induced superconductivity in K_3C_{60}.* ***a.*** *K_3C_{60} unit cell.* ***b.*** *Equilibrium optical conductivity above and below the superconducting transition (T_c = 20 K).* ***c.*** *Resonant mid-infrared excitation of the T_{1u} molecular vibration.* ***d.*** *The terahertz response develops a gapped $\sigma_1(\omega)$ and a $1/\omega$ divergence in $\sigma_2(\omega)$ far above the equilibrium T_c = 20 K. Adapted with permission from Ref. [154]. Copyright (2016) by Springer Nature Limited.*

active H_g Jahn–Teller distortions, which lift the orbital degeneracy of the molecular states and carry the strongest coupling. Mitrano *et al.* therefore excited the $T_{1u}(4)$ mode at 7 µm to drive quasi-static H_g distortion via lowest-order anharmonic coupling, $Q^2_{T_{1u}} Q_{H_g}$ [154]. The transient THz response reproduces the gapped σ_1 and divergent σ_2 of the equilibrium superconductor at base temperatures up to $\sim$ 100 K (Fig. 14), several times T_c, with the photoinduced response fading away at higher temperatures. While the photoinduced gap was slightly larger than that at equilibrium, this driven state showed both the key electrodynamic signatures of a BCS-like superconductor, suggesting a rather homogeneous response.

A series of measurements then tested whether this state follows the expected phenomenology of a BCS superconductor. Cantaluppi *et al.* applied hydrostatic pressure and found that the light-induced gap weakens under compression [155], mirroring the equilibrium superconductor, whose T_c decreases as the bandwidth grows and the density of states falls, and opposite to an ordinary metal, whose conductivity improves under pressure. Wang *et al.* probed the transient state with on-chip ultrafast transport and observed a current-dependent, critical-current-like nonlinearity, characteristic of a superconductor and absent both in the equilibrium metal and under visible-light excitation [156]. Budden *et al.* showed that sustained driving converts the picosecond transient into a metastable state lasting more than ten nanoseconds, with a transport response compatible with vanishing resistance [157], echoing the metastability theme of Sections 4 and 5.3. Finally, Rowe *et al.* mapped the response versus drive frequency and found a pronounced resonant enhancement near 10 THz [158], identifying the spectral region where coupling to the pairing modes is most effective.

Organics. Similar optical responses have also been observed in layered BEDT-TTF-based organic conductors. Unlike the molecular fullerides, the κ-(BEDT-TTF)$_2X$ salts are quasi-two-dimensional and share several defining features with the cuprates. They derive from a half-filled band of (BEDT-TTF)$_2$ dimers on an anisotropic triangular lattice, lie near the boundary between an antiferromagnetic Mott insulator and a superconductor, and show evidence for a $d_{x^2-y^2}$ pairing gap, as in the cuprates [159]. Crucially, their position in the phase diagram can be tuned continuously. In κ-(BEDT-TTF)$_2$Cu[N(CN)$_2$]Br$_x$Cl$_{1-x}$, substituting Cl with Br acts as a bandwidth, or chemical-pressure, knob that drives the system across a bandwidth-controlled Mott transition, from an antiferromagnetic insulator at $x = 0$ to a metallic superconductor at higher Br content [160]. This combination of two-dimensionality, cuprate-like competition between magnetism and pairing, and fine control of correlation strength makes the κ-organics a highly-tunable platform for testing light-induced superconductivity.
Buzzi *et al.* drove molecular C=C vibrations in κ-(BEDT-TTF)$_2$Cu[N(CN)$_2$]Br, the member of the series just on the metallic side of the Mott transition ($T_c = 12.5$ K), and observed a divergent $1/\omega$ response in σ_2, and a gap opening in σ_1 above T_c [161]. The light-induced gap is much larger than, and qualitatively different from, the equilibrium superconducting gap, showing that the driven state is not simply the equilibrium condensate revived above T_c, but a distinct nonequilibrium state. By mapping the entire phase diagram of the family, Buzzi *et al.* also showed that the effect appears only near the Mott boundary, in the metallic compound with strong normal-state superconducting fluctuations, and is absent both in the Mott insulator and in the more itinerant metal farther from the transition [162]. Proximity to the Mott transition, and to the fluctuating precursor it sustains, therefore appears to be a prerequisite for the onset of light-induced superconducting coherence.

A general phenomenon. Taken together, these experiments show that resonant vibrational driving can induce transient superconducting-like responses in very different systems, ranging from layered cuprates to alkali fullerides and organic charge-transfer salts. This phenomenon appears to be general across platforms, and a recurring pattern emerges. Light-induced or enhanced superconductivity is usually found to emerge from strongly fluctuating states near an equilibrium instability, including the stripe-ordered and pseudogap regimes of the cuprates, the Jahn–Teller-correlated metal of K_3C_{60}, and the Mott-proximate organics. This observation suggests that the drive amplifies or reorganizes pre-existing pairing tendencies, rather than creating superconductivity from an inert normal state or relying on structural distortions unique to a given material. Uemura framed this viewpoint in terms of the dynamical response of a phase-incoherent bosonic fluid [163]. The next section reviews the main theoretical scenarios proposed to explain the microscopic origin of this phenomenon.

6.2 Theoretical scenarios

The microscopic mechanism of light-induced superconductivity, and even the precise nature of the transient state, remain open questions. No single theory accounts for all the experimental observations, but the existing proposals fall into a few broad classes.

Lattice-mediated mechanisms. The largest class of theories builds on the nonlinear phononics framework of Section 3.3. The starting point is a resonantly-driven infrared phonon Q_{IR} which rectifies into a quasi-static Raman displacement, $\langle Q_R \rangle \simeq -g \, \langle Q_{\mathrm{IR}}^2 \rangle / \Omega_R^2$, thereby shifting the structural parameters that control the pairing scale [44]. Pairing can then be enhanced in different ways. In the picture of Sentef *et al.*, the distortion narrows the electronic band, reducing the hopping t, increasing the density of states $\bar{N}(E_F)$, and thereby enhancing the dimensionless electron–phonon coupling

$$\lambda = 2 \, \bar{N}(E_F) \int_0^\infty \frac{\alpha^2 F(\Omega)}{\Omega} \, d\Omega, \tag{18}$$

to which the BCS pairing scale is exponentially sensitive [164]. Kennes *et al.* considered instead a *quadratic* electron-phonon coupling, $gK \sum_i \hat{n}_i \hat{x}_i^2$, for which the local phonon frequency depends on the electronic occupation; exciting the phonon to a mean population n_B then renormalizes the effective on-site interaction,

$$U^\star = U - \left(n_B + \tfrac{1}{2}\right) \omega_0 \left(2\sqrt{1{+}2g} - 1 - \sqrt{1{+}4g}\right), \tag{19}$$

where the bracket is positive for either sign of g, so that driving the phonon ($n_B > 0$) lowers $U^\star$ and strengthens the attraction, a purely electronic "squeezing" of the interaction [165]. A third route relies instead on a parametric process. When a coupling is modulated periodically in time, the Cooper-pair fluctuation amplitude obeys, schematically, a Mathieu-type equation

$$\ddot{\Delta}_{\mathbf{q}} + \omega_{\mathbf{q}}^2 \left[\, 1 + \alpha \cos(\Omega t) \,\right] \Delta_{\mathbf{q}} = 0, \tag{20}$$

so that for $\Omega \simeq 2\omega_{\mathbf{q}}$ the pairing susceptibility is parametrically amplified, just as periodically stiffening a pendulum amplifies its swing, without a true equilibrium transition [166]. Related treatments trace the enhancement to nonequilibrium phonon populations that increase the effective coupling [167] or to the transient cooling of the electronic subsystem by mid-infrared absorption [168].

Electronic scenarios. A second class of mechanisms dispenses with the lattice altogether. In the Hubbard model the staggered pair operator

$$\hat{\eta}^+ = \sum_j (-1)^j \, \hat{c}_{j\uparrow}^\dagger \hat{c}_{j\downarrow}^\dagger \tag{21}$$

is an eigenoperator of the Hamiltonian on a bipartite lattice, $[\hat{H}, \hat{\eta}^+] = U\,\hat{\eta}^+$, so the states $(\hat{\eta}^+)^N|0\rangle$ are exact eigenstates with off-diagonal long-range order,

$$\langle \hat{\Delta}_i^\dagger \hat{\Delta}_j \rangle \xrightarrow{|i-j|\to\infty} \text{const} \times e^{\,i\pi(R_i - R_j)}, \qquad \hat{\Delta}_i = \hat{c}_{i\uparrow}\hat{c}_{i\downarrow}, \tag{22}$$

a condensate of pairs carrying center-of-mass momentum $Q = \pi$ [169]. The open question is how to populate these states out of equilibrium. Kaneko *et al.* showed that an optical pulse, entering as a Peierls phase on the hopping, connects η-sectors through the current operator with the selection rule $\Delta\eta = \pm 1$ at an energy cost $\sim U$, so that an intrinsically nonlinear, multi-photon process tuned to $\omega_{\mathrm{pump}} \sim U$ climbs a ladder of η-pairing states [170]. Tindall *et al.* found a complementary route in which heating the spin sector toward infinite temperature, while $\hat{\eta}^+\hat{\eta}^-$ is conserved, forces the charge sector into a steady state with long-range η order [171, 172]. These mechanisms are appealing because they are purely electronic and symmetry-based, in the spirit of the Hamiltonian-engineering route of Section 5.3. However, we need to note that the generated pairs are finite-momentum, a $Q = \pi$ pair-density wave rather than a uniform condensate, and the results rest on the idealized single-band Hubbard model, so their connection to the measured THz response of real solids remains indirect.

Amplification of bosonic excitations or superconducting fluctuations. A particularly compelling proposal, due to Dai and Lee, occupies the middle ground between creating pairs and amplifying an existing condensate [173, 174]. It supposes that charge-$2e$ bosons made of electron pairs are already present in the normal state but remain *gapped* and uncondensed, with dispersion $E_k = \sqrt{\Delta^2 + v^2k^2}$. These bosons could be quantum-fluctuating pairs of the cuprate pseudogap, or the doublon-holon excitations of certain nearly Mott-localized metals. A drive that periodically modulates the boson gap,

$$\mathcal{L} = \tfrac{1}{2}|\partial_t\phi|^2 - \tfrac{v^2}{2}|\nabla\phi|^2 - \tfrac{1}{2}\Delta^2|\phi|^2 - \tfrac{U}{8}|\phi|^4 - \lambda\cos(\Omega t)\,|\phi|^2, \tag{23}$$

then acts as a parametric pump on these bosons. Diagonalizing the driven problem gives complex eigenfrequencies on a resonant ring of momenta,

$$\omega = \frac{\Omega}{2} \pm i\,\theta_k, \qquad \theta_k = \sqrt{\left(\frac{\lambda}{2E_k}\right)^2 - \left(\frac{\Omega}{2} - E_k\right)^2}, \tag{24}$$

so that when the drive satisfies $\Omega \simeq 2E_k$ (hence $\Omega \gtrsim 2\Delta$), boson particle-hole pairs at $\pm k$ are created out of the zero-point fluctuations and grow exponentially. Because of Bose statistics the instability opens not in energy, as for driven fermions, but along a ring in momentum space, building a coherent, two-mode-squeezed "particle-hole condensate." Its oppositely charged components drift in opposite directions under a field, producing precisely the inductive response $\sigma(\omega) = i\,e^{*2}\rho_s/\omega$ of a superconductor, with a transient superfluid density ρ_s that grows and then saturates, even though no equilibrium condensate exists, and, because condensation occurs on a ring rather than at a point, without a Meissner effect. In the variant aimed at the organics, the relevant bosons are the fractionalized charge-e chargons of a metal close to a

Mott transition, and the drive transiently tips the system across that transition; the light-induced "gap" is then reinterpreted as a photoinduced *Mott* gap, a picture that rationalizes why the response in κ-(BEDT-TTF)$_2$Cu[N(CN)$_2$]Br appears only near the transition and is larger than, and distinct from, the equilibrium superconducting gap. Other theoretical scenarios propose amplifying the collective response of pre-existing superconducting fluctuations. A relevant example is the parametric driving of the interlayer Josephson plasmon in a bilayer cuprate, analyzed by Michael *et al.* [175]. The plasma frequency is set by the interlayer Josephson coupling, $\omega_{\mathrm{JP}} \simeq \sqrt{j_c\, d^2(e^*)^2/\epsilon}$, and the resonantly driven apical-oxygen phonon modulates the in-plane superfluid stiffness, introducing a time-periodic term that acts as a parametric drive on the plasmon, exactly the modulation in the Mathieu equation. When the drive frequency matches the sum of two plasmon branches, $\omega_{\mathrm{ph}} = \omega_1 + \omega_2$, the mode amplitudes grow exponentially at a rate $\mathrm{Im}\,\omega = |g\,\xi Q_0|$, and an overdamped plasma edge that is otherwise invisible in equilibrium re-emerges in the transient reflectivity. The result mimics an enhanced superfluid response in $\sigma_2(\omega)$, and reproduces the measured THz signatures, without an increase in T_c or in the number of Cooper pairs.

7 Outlook

The preceding sections offer a necessarily incomplete view of how light control of many-body states has evolved over the past two decades. We close by highlighting three frontiers likely to shape its next stage.

The first is the convergence of ultrafast coherent control with the language of quantum control developed in quantum information science. The quantum control of Hubbard excitons discussed in Section 5.2 illustrates that a single uniaxial $\pi/2$ rotation driven by a mid-infrared field already constitutes the elementary building block of a programmable control sequence [134]. Pulse shaping should extend this approach to Ramsey interferometry, dynamical decoupling, and ultimately full SU(2) control of correlated states [135, 137]. The broader ambition is to treat selected collective excitations of a quantum material as qubit-like degrees of freedom that can be initialized, rotated, entangled, and read out coherently before dissipation takes over. In valleytronics, the coherent encoding and switching of valley information in a WS_2 monolayer at room temperature has already shown that logic operations can be written into a solid on ultrafast timescales [176].

A second frontier is the move from bulk crystals to mesoscale structures and devices. Ultrafast transport, as illustrated by the on-chip detection of a light-induced anomalous Hall effect in graphene [53], measures nonequilibrium currents directly and probes the functional response of a driven material without relying only on the inversion of optical spectra. The next step is to bring this approach to patterned and gated structures, where lithographically defined channels can be used to contact, address, and integrate light-engineered states. Van der Waals materials and heterostructures are especially well suited to this program. They are atomically thin, electrostatically tunable, and freely stackable, allowing driving, gating, and transport readout to be combined in a single device, while interactions are tuned *in situ* across phase boundaries.

The third, and conceptually most far-reaching, frontier is the control of quantum materials through their electromagnetic environment, by embedding them in optical cavities [177]. Cavity-mediated control of the metal-to-insulator transition in 1T-TaS_2 [178], and cavity-induced, exciton-like attraction observed in bilayer graphene ultrastrongly coupled to a terahertz resonator [179] show that the electromagnetic environment alone can reorganize electronic response. Extending this idea to superconductivity is a compelling emergent direction, with first reports of a cavity-enhanced superconducting response in an underdoped cuprate [180] and of an enhanced transition temperature in few-layer $NbSe_2$ tuned to a phononic cavity mode [181]. These results connect cavity engineering directly to the light-induced superconducting responses discussed in Section 6.

A crucial conceptual distinction in the possible implementations of cavity experiments is that between *driven* and *dark* cavities. In the former, light still injects energy into the material, even if the cavity reshapes the electromagnetic modes through which this occurs. In the latter, no external photons are involved, and the material is solely modified by the vacuum fluctuations of the confined field, enhanced at the cavity resonances. The breakdown of topological protection in the integer quantum Hall effect induced by cavity vacuum fields in a Hall-bar geometry [182], together with the recent observation of a cavity-altered superconducting ground state at a hexagonal boron nitride interface [183], shows that an electromagnetic environment can reshape a many-body state without a drive. This development addresses a central limitation of many driven protocols reviewed in this chapter, namely the heating and dissipation that accompany continuous excitation and limit the lifetime of the engineered state. A dark cavity does not push the system into a transient excited configuration, rather it modifies the *ground state* itself. Whether vacuum fields can be made strong enough to engineer correlated ground states at will remains an open question. But the possibility of equilibrium, dissipation-free control of many-body states is, in our view, one of the most exciting prospects for the field.

Acknowledgments

Part of the work described in the manuscript is the result of the author's collaboration with many researchers listed in the references below. The author is especially grateful to Michele Buzzi, Ankit Disa, Michael Först, Anshul Kogar, Roman Mankowsky, Michael A. Sentef, and Mariano Trigo for discussions and input on the manuscript, as well as to Brad Baxley for assistance with graphics.

References

[1] J. Zhang and R. Averitt, Ann. Rev. Mater. Res. **44**, 19 (2014)

[2] C. Giannetti, M. Capone, D. Fausti, M. Fabrizio, F. Parmigiani, and D. Mihailovic, Adv. Phys. **65**, 58 (2016)

[3] D.N. Basov, R.D. Averitt, and D. Hsieh, Nat. Mater. **16**, 1077 (2017)

[4] A. de la Torre, D.M. Kennes, M. Claassen, S. Gerber, J.W. McIver, and M.A. Sentef, Rev. Mod. Phys. **93**, 041002 (2021)

[5] J. Bloch, A. Cavalleri, V. Galitski, M. Hafezi, and A. Rubio, Nature **606**, 41 (2022)

[6] K. Nasu: *Photoinduced Phase Transitions* (World Scientific, 2004)

[7] R.D. Averitt and A.J. Taylor, J. Phys.: Condens. Matter **14**, R1357 (2002)

[8] B. Keimer and J.E. Moore, Nat. Phys. **13**, 1045 (2017)

[9] G. Steinmeyer, D.H. Sutter, L. Gallmann, N. Matuschek, and U. Keller, Science **286**, 1507 (1999)

[10] R.A. Bartels, A. Paul, H. Green, H.C. Kapteyn, M.M. Murnane, S. Backus, I.P. Christov, Y. Liu, D. Attwood, and C. Jacobsen, Science **297**, 376 (2002)

[11] G. Cerullo and S. De Silvestri, Rev. Sci. Instr. **74**, 1 (2003)

[12] K. Reimann, Rep. Prog. Phys. **70**, 1597 (2007)

[13] B. Liu, H. Bromberger, A. Cartella, T. Gebert, M. Först, and A. Cavalleri, Opt. Lett. **42**, 129 (2017)

[14] J. Orenstein, Physics Today **65**, 44 (2012)

[15] R.W. Schoenlein, W.Z. Lin, J.G. Fujimoto, and G.L. Eesley, Phys. Rev. Lett. **58**, 1680 (1987)

[16] S. Koshihara, Y. Tokura, T. Mitani, G. Saito, and T. Koda, Phys. Rev. B **42**, 6853(R) (1990)

[17] S.D. Brorson, A. Kazeroonian, J.S. Moodera, D.W. Face, T.K. Cheng, E.P. Ippen, M.S. Dresselhaus, and G. Dresselhaus, Phys. Rev. Lett. **64**, 2172 (1990)

[18] J. Demsar, B. Podobnik, V.V. Kabanov, T. Wolf, and D. Mihailovic, Phys. Rev. Lett. **82**, 4918 (1999)

[19] D.S. Chemla and J. Shah, Proc. Natl. Acad. Sci. USA **97**, 2437 (2000)

[20] A. Kirilyuk, A.V. Kimel, and T. Rasing, Rev. Mod. Phys. **82**, 2731 (2010)

[21] S.L. Dexheimer (Ed.): *Terahertz Spectroscopy: Principles and Applications* (CRC Press, 2008), 1st ed.

[22] S. Ghimire and D.A. Reis, Nat. Phys. **15**, 10 (2019)

[23] L. Zhao, D. Torchinsky, J. Harter, A. de la Torre, and D. Hsieh, in B.D. Guenther and D.G. Steel (eds.): *Encyclopedia of Modern Optics (2nd Ed.)* (Elsevier, 2018), p. 207

[24] M. Fiebig, K. Miyano, Y. Tomioka, and Y. Tokura, Science **280**, 1925 (1998)

[25] T.F. Nova, A.S. Disa, M. Fechner, and A. Cavalleri, Science **364**, 1075 (2019)

[26] X. Zhang, T. Carbin, A.B. Culver, K. Du, K. Wang, S.-W. Cheong, R. Roy, and A. Kogar, Nat. Mater. **23**, 790 (2024)

[27] F. Boschini, M. Zonno, and A. Damascelli, Rev. Mod. Phys. **96**, 015003 (2024)

[28] I. Gierz, J.C. Petersen, M. Mitrano, C. Cacho, I.C.E. Turcu, E. Springate, A. Stöhr, A. Köhler, U. Starke, and A. Cavalleri, Nat. Mater. **12**, 1119 (2013)

[29] U. Höfer, I.L. Shumay, C. Reuß, U. Thomann, W. Wallauer, and T. Fauster, Science **277**, 1480 (1997)

[30] S. Gerber, S.-L. Yang, D. Zhu, H. Soifer, J.A. Sobota, S. Rebec, J.J. Lee, T. Jia, B. Moritz, C. Jia, A. Gauthier, Y. Li, D. Leuenberger, Y. Zhang, L. Chaix, W. Li, H. Jang, J.-S. Lee, M. Yi, G.L. Dakovski, S. Song, J.M. Glownia, S. Nelson, K.W. Kim, Y.-D. Chuang, Z. Hussain, R.G. Moore, T.P. Devereaux, W.-S. Lee, P.S. Kirchmann, and Z.-X. Shen, Science **357**, 71 (2017)

[31] C.L. Smallwood, J.P. Hinton, C. Jozwiak, W. Zhang, J.D. Koralek, H. Eisaki, D.-H. Lee, J. Orenstein, and A. Lanzara, Science **336**, 1137 (2012)

[32] T. Rohwer, S. Hellmann, M. Wiesenmayer, C. Sohrt, A. Stange, B. Slomski, A. Carr, Y. Liu, L.M. Avila, M. Kalläne, S. Mathias, L. Kipp, K. Rossnagel, and M. Bauer, Nature **471**, 490 (2011)

[33] J.C. Petersen, S. Kaiser, N. Dean, A. Simoncig, H.Y. Liu, A.L. Cavalieri, C. Cacho, I.C.E. Turcu, E. Springate, F. Frassetto, L. Poletto, S.S. Dhesi, H. Berger, and A. Cavalleri, Phys. Rev. Lett. **107**, 177402 (2011)

[34] Y.H. Wang, H. Steinberg, P. Jarillo-Herrero, and N. Gedik, Science **342**, 453 (2013)

[35] F. Mahmood, C. Chan, Z. Alpichshev, D. Gardner, Y. Lee, and N. Gedik, Nat. Phys. **12**, 306 (2016)

[36] S. Ito, M. Schüler, M. Meierhofer, S. Schlauderer, J. Freudenstein, J. Reimann, D. Afanasiev, K.A. Kokh, O.E. Tereshchenko, J. Güdde, M.A. Sentef, U. Höfer, and R. Huber, Nature **616**, 696 (2023)

[37] N. Bielinski, R. Chari, J. May-Mann, S. Kim, J. Zwettler, Y. Deng, A. Aishwarya, S. Roychowdhury, C. Shekhar, M. Hashimoto, D. Lu, J. Yan, C. Felser, V. Madhavan, Z.-X. Shen, T.L. Hughes, and F. Mahmood, Nat. Phys. **21**, 458 (2025)

[38] P. Emma, R. Akre, J. Arthur, R. Bionta, C. Bostedt, J. Bozek, A. Brachmann, P. Bucksbaum, R. Coffee, F.-J. Decker, Y. Ding, D. Dowell, S. Edstrom, A. Fisher, J. Frisch, S. Gilevich, J. Hastings, G. Hays, P. Hering, Z. Huang, R. Iverson, H. Loos, M. Messerschmidt, A. Miahnahri, S. Moeller, H.-D. Nuhn, G. Pile, D. Ratner, J. Rzepiela, D. Schultz, T. Smith, P. Stefan, H. Tompkins, J. Turner, J. Welch, W. White, J. Wu, G. Yocky, and J. Galayda, Nat. Photonics **4**, 641 (2010)

[39] S.P. Weathersby, G. Brown, M. Centurion, T.F. Chase, R. Coffee, J. Corbett, J.P. Eichner, J.C. Frisch, A.R. Fry, M. Gühr, N. Hartmann, C. Hast, R. Hettel, R.K. Jobe, E.N. Jongewaard, J.R. Lewandowski, R.K. Li, A.M. Lindenberg, I. Makasyuk, J.E. May, D. McCormick, M.N. Nguyen, A.H. Reid, X. Shen, K. Sokolowski-Tinten, T. Vecchione, S.L. Vetter, J. Wu, J. Yang, H.A. Dürr, and X.J. Wang, Rev. Sci. Instr. **86**, 073702 (2015)

[40] K. Sokolowski-Tinten, C. Blome, J. Blums, A. Cavalleri, C. Dietrich, A. Tarasevitch, I. Uschmann, E. Förster, M. Kammler, M. Horn-von Hoegen, and D. von der Linde, Nature **422**, 287 (2003)

[41] D.M. Fritz, D.A. Reis, B. Adams, R.A. Akre, J. Arthur, C. Blome, P.H. Bucksbaum, A.L. Cavalieri, S. Engemann, S. Fahy, R.W. Falcone, P.H. Fuoss, K.J. Gaffney, M.J. George, J. Hajdu, M.P. Hertlein, P.B. Hillyard, M.H. von Hoegen, M. Kammler, J. Kaspar, R. Kienberger, P. Krejcik, S.H. Lee, A.M. Lindenberg, B. McFarland, D. Meyer, T. Montagne, E.D. Murray, A.J. Nelson, M. Nicoul, R. Pahl, J. Rudati, H. Schlarb, D.P. Siddons, K. Sokolowski-Tinten, T. Tschentscher, D. von der Linde, and J.B. Hastings, Science **315**, 633 (2007)

[42] P. Baum, D.-S. Yang, and A.H. Zewail, Science **318**, 788 (2007)

[43] P. Beaud, A. Caviezel, S.O. Mariager, L. Rettig, G. Ingold, C. Dornes, S.-W. Huang, J.A. Johnson, M. Radovic, T. Huber, T. Kubacka, A. Ferrer, H.T. Lemke, M. Chollet, D. Zhu, J.M. Glownia, M. Sikorski, A. Robert, H. Wadati, M. Nakamura, M. Kawasaki, Y. Tokura, S.L. Johnson, and U. Staub, Nat. Mater. **13**, 923 (2014)

[44] R. Mankowsky, A. Subedi, M. Först, S.O. Mariager, M. Chollet, H.T. Lemke, J.S. Robinson, J.M. Glownia, M.P. Minitti, A. Frano, M. Fechner, N.A. Spaldin, T. Loew, B. Keimer, A. Georges, and A. Cavalleri, Nature **516**, 71 (2014)

[45] S. Wall, S. Yang, L. Vidas, M. Chollet, J.M. Glownia, M. Kozina, T. Katayama, T. Henighan, M. Jiang, T.A. Miller, D.A. Reis, L.A. Boatner, O. Delaire, and M. Trigo, Science **362**, 572 (2018)

[46] S. Vogelgesang, G. Storeck, J.G. Horstmann, T. Diekmann, M. Sivis, S. Schramm, K. Rossnagel, S. Schäfer, and C. Ropers, Nat. Phys. **14**, 184 (2018)

[47] A. Kogar, A. Zong, P.E. Dolgirev, X. Shen, J. Straquadine, Y.-Q. Bie, X. Wang, T. Rohwer, I.-C. Tung, Y. Yang, R. Li, J. Yang, S. Weathersby, S. Park, M.E. Kozina, E.J. Sie, H. Wen, P. Jarillo-Herrero, I.R. Fisher, X. Wang, and N. Gedik, Nat. Phys. **16**, 159 (2020)

[48] M.P.M. Dean, Y. Cao, X. Liu, S. Wall, D. Zhu, R. Mankowsky, V. Thampy, X.M. Chen, J.G. Vale, D. Casa, J. Kim, A.H. Said, P. Juhas, R. Alonso-Mori, J.M. Glownia, A. Robert, J. Robinson, M. Sikorski, S. Song, M. Kozina, H. Lemke, L. Patthey, S. Owada, T. Katayama, M. Yabashi, Y. Tanaka, T. Togashi, J. Liu, C. Rayan Serrao, B.J. Kim, L. Huber, C.-L. Chang, D.F. McMorrow, M. Först, and J.P. Hill, Nat. Mater. **15**, 601 (2016)

[49] H. Padma, F. Glerean, S.F.R. TenHuisen, Z. Shen, H. Wang, L. Xu, J.D. Elliott, C.C. Homes, E. Skoropata, H. Ueda, B. Liu, E. Paris, A. Romaguera, B. Lee, W. He, Y. Wang, S.H. Lee, H. Choi, S.-Y. Park, Z. Mao, M. Calandra, H. Jang, E. Razzoli, M.P.M. Dean, Y. Wang, and M. Mitrano, Nat. Mater. **24**, 1584 (2025)

[50] T.L. Cocker, V. Jelic, M. Gupta, S.J. Molesky, J.A.J. Burgess, G. De Los Reyes, L.V. Titova, Y.Y. Tsui, M.R. Freeman, and F.A. Hegmann, Nat. Photonics **7**, 620 (2013)

[51] T.L. Cocker, D. Peller, P. Yu, J. Repp, and R. Huber, Nature **539**, 263 (2016)

[52] M. Wagner, Z. Fei, A.S. McLeod, A.S. Rodin, W. Bao, E.G. Iwinski, Z. Zhao, M. Goldflam, M. Liu, G. Dominguez, M. Thiemens, M.M. Fogler, A.H. Castro Neto, C.N. Lau, S. Amarie, F. Keilmann, and D.N. Basov, Nano Lett. **14**, 894 (2014)

[53] J.W. McIver, B. Schulte, F.-U. Stein, T. Matsuyama, G. Jotzu, G. Meier, and A. Cavalleri, Nat. Phys. **16**, 38 (2020)

[54] H. Aoki, N. Tsuji, M. Eckstein, M. Kollar, T. Oka, and P. Werner, Rev. Mod. Phys. **86**, 779 (2014)

[55] Y. Murakami, D. Golež, M. Eckstein, and P. Werner, Rev. Mod. Phys. **97**, 035001 (2025)

[56] A. Georges, G. Kotliar, W. Krauth, and M.J. Rozenberg, Rev. Mod. Phys. **68**, 13 (1996)

[57] D.I. Khomskii: *Transition Metal Compounds* (Cambridge University Press, 2014)

[58] J. Zaanen, G.A. Sawatzky, and J.W. Allen, Phys. Rev. Lett. **55**, 418 (1985)

[59] H. Okamoto, H. Matsuzaki, T. Wakabayashi, Y. Takahashi, and T. Hasegawa, Phys. Rev. Lett. **98**, 037401 (2007)

[60] S. Wall, D. Brida, S.R. Clark, H.P. Ehrke, D. Jaksch, A. Ardavan, S. Bonora, H. Uemura, Y. Takahashi, T. Hasegawa, H. Okamoto, G. Cerullo, and A. Cavalleri, Nat. Phys. **7**, 114 (2011)

[61] M. Mitrano, G. Cotugno, S.R. Clark, R. Singla, S. Kaiser, J. Stähler, R. Beyer, M. Dressel, L. Baldassarre, D. Nicoletti, A. Perucchi, T. Hasegawa, H. Okamoto, D. Jaksch, and A. Cavalleri, Phys. Rev. Lett. **112**, 117801 (2014)

[62] T. Ishikawa, Y. Sagae, Y. Naitoh, Y. Kawakami, H. Itoh, K. Yamamoto, K. Yakushi, H. Kishida, T. Sasaki, S. Ishihara, Y. Tanaka, K. Yonemitsu, and S. Iwai, Nat. Commun. **5**, 5528 (2014)

[63] H. Okamoto, T. Miyagoe, K. Kobayashi, H. Uemura, H. Nishioka, H. Matsuzaki, A. Sawa, and Y. Tokura, Phys. Rev. B **83**, 125102 (2011)

[64] E. Baldini, M.A. Sentef, S. Acharya, T. Brumme, E. Sheveleva, F. Lyzwa, E. Pomjakushina, C. Bernhard, M. van Schilfgaarde, F. Carbone, A. Rubio, and C. Weber, Proc. Natl. Acad. Sci. USA **117**, 6409 (2020)

[65] F.J. Morin, Phys. Rev. Lett. **3**, 34 (1959)

[66] A. Cavalleri, C. Tóth, C.W. Siders, J.A. Squier, F. Ráksi, P. Forget, and J.C. Kieffer, Phys. Rev. Lett. **87**, 237401 (2001)

[67] S. Wall, D. Wegkamp, L. Foglia, K. Appavoo, J. Nag, J. Haglund, Jr., J. Stähler, and M. Wolf, Nat. Commun. **3**, 721 (2012)

[68] V.R. Morrison, R.P. Chatelain, K.L. Tiwari, A. Hendaoui, A. Bruhács, M. Chaker, and B.J. Siwick, Science **346**, 445 (2014)

[69] H.J. Zeiger, J. Vidal, T.K. Cheng, E.P. Ippen, G. Dresselhaus, and M.S. Dresselhaus, Phys. Rev. B **45**, 768 (1992)

[70] R. Merlin, Solid State Commun. **102**, 207 (1997)

[71] A.S. Disa, T.F. Nova, and A. Cavalleri, Nat. Phys. **17**, 1087 (2021)

[72] M. Rini, R. Tobey, N. Dean, J. Itatani, Y. Tomioka, Y. Tokura, R.W. Schoenlein, and A. Cavalleri, Nature **449**, 72 (2007)

[73] M. Först, C. Manzoni, S. Kaiser, Y. Tomioka, Y. Tokura, R. Merlin, and A. Cavalleri, Nat. Phys. **7**, 854 (2011)

[74] A. Subedi, A. Cavalleri, and A. Georges, Phys. Rev. B **89**, 220301 (2014)

[75] A.D. Caviglia, R. Scherwitzl, P. Popovich, W. Hu, H. Bromberger, R. Singla, M. Mitrano, M.C. Hoffmann, S. Kaiser, P. Zubko, S. Gariglio, J.-M. Triscone, M. Först, and A. Cavalleri, Phys. Rev. Lett. **108**, 136801 (2012)

[76] G. Grüner: *Density Waves in Solids* (CRC Press, 1994), 1st ed.

[77] S. Hellmann, T. Rohwer, M. Kalläne, K. Hanff, C. Sohrt, A. Stange, A. Carr, M.M. Murnane, H.C. Kapteyn, L. Kipp, M. Bauer, and K. Rossnagel, Nat. Commun. **3**, 1069 (2012)

[78] T. Huber, S.O. Mariager, A. Ferrer, H. Schäfer, J.A. Johnson, S. Grübel, A. Lübcke, L. Huber, T. Kubacka, C. Dornes, C. Laulhe, S. Ravy, G. Ingold, P. Beaud, J. Demsar, and S.L. Johnson, Phys. Rev. Lett. **113**, 026401 (2014)

[79] H.Y. Liu, I. Gierz, J.C. Petersen, S. Kaiser, A. Simoncig, A.L. Cavalieri, C. Cacho, I.C.E. Turcu, E. Springate, F. Frassetto, L. Poletto, S.S. Dhesi, Z.-A. Xu, T. Cuk, R. Merlin, and A. Cavalleri, Phys. Rev. B **88**, 045104 (2013)

[80] L. Stojchevska, I. Vaskivskyi, T. Mertelj, P. Kusar, D. Svetin, S. Brazovskii, and D. Mihailovic, Science **344**, 177 (2014)

[81] M. Mitrano, S. Lee, A.A. Husain, L. Delacretaz, M. Zhu, G. de la Peña Munoz, S.X.-L. Sun, Y.I. Joe, A.H. Reid, S.F. Wandel, G. Coslovich, W. Schlotter, T. van Driel, J. Schneeloch, G.D. Gu, S. Hartnoll, N. Goldenfeld, and P. Abbamonte, Sci. Adv. **5**, eaax3346 (2019)

[82] B. Keimer, S.A. Kivelson, M.R. Norman, S. Uchida, and J. Zaanen, Nature **518**, 179 (2015)

[83] R. Comin and A. Damascelli, Ann. Rev. Condens. Matter Phys. **7**, 369 (2016)

[84] D.F. Agterberg, J.S. Davis, S.D. Edkins, E. Fradkin, D.J. Van Harlingen, S.A. Kivelson, P.A. Lee, L. Radzihovsky, J.M. Tranquada, and Y. Wang, Ann. Rev. Condens. Matter Phys. **11**, 231 (2020)

[85] M. Först, R.I. Tobey, H. Bromberger, S.B. Wilkins, V. Khanna, A.D. Caviglia, Y.-D. Chuang, W.S. Lee, W.F. Schlotter, J.J. Turner, M.P. Minitti, O. Krupin, Z.J. Xu, J.S. Wen, G.D. Gu, S.S. Dhesi, A. Cavalleri, and J.P. Hill, Phys. Rev. Lett. **112**, 157002 (2014)

[86] M. Mitrano, S. Lee, A.A. Husain, M. Zhu, G. de la Peña Muñoz, S.X.-L. Sun, Y.I. Joe, A.H. Reid, S.F. Wandel, G. Coslovich, W. Schlotter, T. van Driel, J. Schneeloch, G.D. Gu, N. Goldenfeld, and P. Abbamonte, Phys. Rev. B **100**, 205125 (2019)

[87] S. Wandel, F. Boschini, E.H. da Silva Neto, L. Shen, M.X. Na, S. Zohar, Y. Wang, S.B. Welch, M.H. Seaberg, J.D. Koralek, G.L. Dakovski, W. Hettel, M.-F. Lin, S.P. Moeller, W.F. Schlotter, A.H. Reid, M.P. Minitti, T. Boyle, F. He, R. Sutarto,

R. Liang, D. Bonn, W. Hardy, R.A. Kaindl, D.G. Hawthorn, J.-S. Lee, A.F. Kemper, A. Damascelli, C. Giannetti, J.J. Turner, and G. Coslovich, Science **376**, 860 (2022)

[88] E. Beaurepaire, J.-C. Merle, A. Daunois, and J.-Y. Bigot, Phys. Rev. Lett. **76**, 4250 (1996)

[89] A.V. Kimel, A. Kirilyuk, P.A. Usachev, R.V. Pisarev, A.M. Balbashov, and T. Rasing, Nature **435**, 655 (2005)

[90] T. Kampfrath, A. Sell, G. Klatt, A. Pashkin, S. Mährlein, T. Dekorsy, M. Wolf, M. Fiebig, A. Leitenstorfer, and R. Huber, Nat. Photonics **5**, 31 (2011)

[91] C.D. Stanciu, F. Hansteen, A.V. Kimel, A. Kirilyuk, A. Tsukamoto, A. Itoh, and T. Rasing, Phys. Rev. Lett. **99**, 047601 (2007)

[92] A. Stupakiewicz, C.S. Davies, K. Szerenos, D. Afanasiev, K.S. Rabinovich, A.V. Boris, A.D. Caviglia, A.V. Kimel, and A. Kirilyuk, Nat. Phys. **17**, 489 (2021)

[93] I. Radu, K. Vahaplar, C. Stamm, T. Kachel, N. Pontius, H.A. Dürr, T.A. Ostler, J. Barker, R.F.L. Evans, R.W. Chantrell, A. Tsukamoto, A. Itoh, A. Kirilyuk, T. Rasing, and A.V. Kimel, Nature **472**, 205 (2011)

[94] D. Afanasiev, J.R. Hortensius, B.A. Ivanov, A. Sasani, E. Bousquet, Y.M. Blanter, R.V. Mikhaylovskiy, A.V. Kimel, and A.D. Caviglia, Nat. Mater. **20**, 607 (2021)

[95] T.F. Nova, A. Cartella, A. Cantaluppi, M. Först, D. Bossini, R.V. Mikhaylovskiy, A.V. Kimel, R. Merlin, and A. Cavalleri, Nat. Phys. **13**, 132 (2017)

[96] D.M. Juraschek, M. Fechner, A.V. Balatsky, and N.A. Spaldin, Phys. Rev. Mater. **1**, 014401 (2017)

[97] D.M. Juraschek, P. Narang, and N.A. Spaldin, Phys. Rev. Res. **2**, 043035 (2020)

[98] D.M. Juraschek, T. Neuman, and P. Narang, Phys. Rev. Res. **4**, 013129 (2022)

[99] J. Luo, T. Lin, J. Zhang, X. Chen, E.R. Blackert, R. Xu, B.I. Yakobson, and H. Zhu, Science **382**, 698 (2023)

[100] A.S. Disa, M. Fechner, T.F. Nova, B. Liu, M. Först, D. Prabhakaran, P.G. Radaelli, and A. Cavalleri, Nat. Phys. **16**, 937 (2020)

[101] A.S. Disa, J. Curtis, M. Fechner, A. Liu, A. von Hoegen, M. Först, T.F. Nova, P. Narang, A. Maljuk, A.V. Boris, B. Keimer, and A. Cavalleri, Nature **617**, 73 (2023)

[102] B. Ilyas, T. Luo, A. von Hoegen, E. Viñas Boström, Z. Zhang, J. Park, J. Kim, J.-G. Park, K.A. Nelson, A. Rubio, and N. Gedik, Nature **636**, 609 (2024)

[103] R. Mankowsky, A. von Hoegen, M. Först, and A. Cavalleri, Phys. Rev. Lett. **118**, 197601 (2017)

[104] G. Orenstein, V. Krapivin, Y. Huang, Z. Zhang, G. de la Peña Muñoz, R.A. Duncan, Q. Nguyen, J. Stanton, S. Teitelbaum, H. Yavas, T. Sato, M.C. Hoffmann, P. Kramer, J. Zhang, A. Cavalleri, R. Comin, M.P.M. Dean, A.S. Disa, M. Först, S.L. Johnson, M. Mitrano, A.M. Rappe, D.A. Reis, D. Zhu, K.A. Nelson, and M. Trigo, Nat. Phys. **21**, 961 (2025)

[105] X. Li, T. Qiu, J. Zhang, E. Baldini, J. Lu, A.M. Rappe, and K.A. Nelson, Science **364**, 1079 (2019)

[106] M. Fechner, M. Först, G. Orenstein, V. Krapivin, A.S. Disa, M. Buzzi, A. von Hoegen, G. de la Pena, Q.L. Nguyen, R. Mankowsky, M. Sander, H. Lemke, Y. Deng, M. Trigo, and A. Cavalleri, Nat. Mater. **23**, 363 (2024)

[107] H.H. Wang, M. Fechner, G. De Vecchi, S.L. Griffitt, G. Orenstein, J. Stanton, V. Krapivin, M.T. Wong, Z. Zhang, M. Bionta, V. Esposito, M. Henstridge, M.C. Hoffmann, P.L. Kramer, Z. Porter, R.A. Duncan, T. Sato, S.K. Kim, H. Yavas, S. Teitelbaum, K. Nelson, A.S. Disa, M. Först, M. Trigo, and A. Cavalleri, arXiv:2606.16267 (2026)

[108] T. Kubacka, J.A. Johnson, M.C. Hoffmann, C. Vicario, S. de Jong, P. Beaud, S. Grübel, S.-W. Huang, L. Huber, L. Patthey, Y.-D. Chuang, J.J. Turner, G.L. Dakovski, W.-S. Lee, M.P. Minitti, W. Schlotter, R.G. Moore, C.P. Hauri, S.M. Koohpayeh, V. Scagnoli, G. Ingold, S.L. Johnson, and U. Staub, Science **343**, 1333 (2014)

[109] Z. Zeng, M. Först, M. Fechner, D. Prabhakaran, P.G. Radaelli, and A. Cavalleri, Science **390**, 195 (2025)

[110] S.H. Autler and C.H. Townes, Phys. Rev. **100**, 703 (1955)

[111] T. Oka and S. Kitamura, Ann. Rev. Condens. Matter Phys. **10**, 387 (2019)

[112] M.S. Rudner and N.H. Lindner, Nat. Rev. Phys. **2**, 229 (2020)

[113] D.H. Dunlap and V.M. Kenkre, Phys. Rev. B **34**, 3625 (1986)

[114] J.H. Mentink, K. Balzer, and M. Eckstein, Nat. Commun. **6**, 6708 (2015)

[115] G. Floquet, Annales scientifiques de l'École Normale Supérieure **12**, 47 (1883)

[116] M. Bukov, L. D'Alessio, and A. Polkovnikov, Adv. Phys. **64**, 139 (2015)

[117] T. Oka and H. Aoki, Phys. Rev. B **79**, 081406(R) (2009)

[118] N.H. Lindner, G. Refael, and V. Galitski, Nat. Phys. **7**, 490 (2011)

[119] T. Kitagawa, T. Oka, A. Brataas, L. Fu, and E. Demler, Phys. Rev. B **84**, 235108 (2011)

[120] S. Zhou, C. Bao, B. Fan, H. Zhou, Q. Gao, H. Zhong, T. Lin, H. Liu, P. Yu, P. Tang, S. Meng, W. Duan, and S. Zhou, Nature **614**, 75 (2023)

[121] D. Choi, M. Mogi, U. De Giovannini, D. Azoury, B. Lv, Y. Su, H. Hübener, A. Rubio, and N. Gedik, Nat. Phys. **21**, 1100 (2025)

[122] M. Merboldt, M. Schüler, D. Schmitt, J.P. Bange, W. Bennecke, K. Gadge, K. Pierz, H.W. Schumacher, D. Momeni, D. Steil, S.R. Manmana, M.A. Sentef, M. Reutzel, and S. Mathias, Nat. Phys. **21**, 1093 (2025)

[123] E.J. Sie, J.W. McIver, Y.-H. Lee, L. Fu, J. Kong, and N. Gedik, Nat. Mater. **14**, 290 (2015)

[124] E.J. Sie, C.H. Lui, Y.-H. Lee, L. Fu, J. Kong, and N. Gedik, Science **355**, 1066 (2017)

[125] J.-Y. Shan, M. Ye, H. Chu, S. Lee, J.-G. Park, L. Balents, and D. Hsieh, Nature **600**, 235 (2021)

[126] S.T. Cundiff, A. Knorr, J. Feldmann, S.W. Koch, E.O. Göbel, and H. Nickel, Phys. Rev. Lett. **73**, 1178 (1994)

[127] B.E. Cole, J.B. Williams, B.T. King, M.S. Sherwin, and C.R. Stanley, Nature **410**, 60 (2001)

[128] D. Press, T.D. Ladd, B. Zhang, and Y. Yamamoto, Nature **456**, 218 (2008)

[129] J. Berezovsky, M.H. Mikkelsen, N.G. Stoltz, L.A. Coldren, and D.D. Awschalom, Science **320**, 349 (2008)

[130] D.G. Clarke, Phys. Rev. B **48**, 7520 (1993)

[131] F.H.L. Essler, F. Gebhard, and E. Jeckelmann, Phys. Rev. B **64**, 125119 (2001)

[132] H. Kishida, H. Matsuzaki, H. Okamoto, T. Manabe, M. Yamashita, Y. Taguchi, and Y. Tokura, Nature **405**, 929 (2000)

[133] M. Ono, K. Miura, A. Maeda, H. Matsuzaki, H. Kishida, Y. Taguchi, Y. Tokura, M. Yamashita, and H. Okamoto, Phys. Rev. B **70**, 085101 (2004)

[134] D.R. Baykusheva, D. Carmichael, C.S. Weber, I.-T. Lu, F. Glerean, T. Meng, P.B.M. De Oliveira, C.C. Homes, I.A. Zaliznyak, G.D. Gu, M.P.M. Dean, A. Rubio, D.M. Kennes, M. Claassen, and M. Mitrano, Nat. Mater. **25**, 937 (2026)

[135] H.A. Rabitz, M.M. Hsieh, and C.M. Rosenthal, Science **303**, 1998 (2004)

[136] L.M.K. Vandersypen and I.L. Chuang, Rev. Mod. Phys. **76**, 1037 (2005)

[137] J. Choi, H. Zhou, H.S. Knowles, R. Landig, S. Choi, and M.D. Lukin, Phys. Rev. X **10**, 031002 (2020)

[138] H. Padma, P. Sharma, S.F.R. TenHuisen, F. Glerean, A. Roll, P. Zhou, S. Kundu, A. Romaguera, E. Skoropata, H. Ueda, B. Liu, E. Paris, Y. Wang, S.H. Lee, Z. Mao, M.P.M. Dean, E.W. Huang, E. Razzoli, Y. Wang, and M. Mitrano, Phys. Rev. Lett. **136**, 196501 (2026)

[139] R.D. Averitt, G. Rodriguez, A.I. Lobad, J.L.W. Siders, S.A. Trugman, and A.J. Taylor, Phys. Rev. B **63**, 140502 (2001)

[140] R.A. Kaindl, M. Woerner, T. Elsaesser, D.C. Smith, J.F. Ryan, G.A. Farnan, M.P. McCurry, and D.G. Walmsley, Science **287**, 470 (2000)

[141] A. Pashkin, M. Porer, M. Beyer, K.W. Kim, A. Dubroka, C. Bernhard, X. Yao, Y. Dagan, R. Hackl, A. Erb, J. Demsar, R. Huber, and A. Leitenstorfer, Phys. Rev. Lett. **105**, 067001 (2010)

[142] J. Demsar, J. Low Temp. Phys. **201**, 676 (2020)

[143] A.F.G. Wyatt, V.M. Dmitriev, W.S. Moore, and F.W. Sheard, Phys. Rev. Lett. **16**, 1166 (1966)

[144] A.H. Dayem and J.J. Wiegand, Phys. Rev. **155**, 419 (1967)

[145] G.M. Eliashberg, JETP Lett. **11**, 114 (1970) [Pis'ma Zh. Eksp. Teor. Fiz. **11**, 186 (1970)]

[146] M. Dressel and G. Grüner: *Electrodynamics of Solids: Optical Properties of Electrons in Matter* (Cambridge University Press, 2002)

[147] M. Tinkham: *Introduction to Superconductivity* (Dover Publications, 2004), 2nd ed.

[148] S. Fava, G. De Vecchi, G. Jotzu, M. Buzzi, T. Gebert, Y. Liu, B. Keimer, and A. Cavalleri, Nature **632**, 75 (2024)

[149] D. Fausti, R. Tobey, N. Dean, S. Kaiser, A. Dienst, M.C. Hoffmann, S. Pyon, T. Takayama, H. Takagi, and A. Cavalleri, Science **331**, 189 (2011)

[150] E. Pavarini, I. Dasgupta, T. Saha-Dasgupta, O. Jepsen, and O.K. Andersen, Phys. Rev. Lett. **87**, 047003 (2001)

[151] W. Hu, S. Kaiser, D. Nicoletti, C.R. Hunt, I. Gierz, M.C. Hoffmann, M. Le Tacon, T. Loew, B. Keimer, and A. Cavalleri, Nat. Mater. **13**, 705 (2014)

[152] S. Kaiser, C.R. Hunt, D. Nicoletti, W. Hu, I. Gierz, H.Y. Liu, M. Le Tacon, T. Loew, D. Haug, B. Keimer, and A. Cavalleri, Phys. Rev. B **89**, 184516 (2014)

[153] O. Gunnarsson, Rev. Mod. Phys. **69**, 575 (1997)

[154] M. Mitrano, A. Cantaluppi, D. Nicoletti, S. Kaiser, A. Perucchi, S. Lupi, P. Di Pietro, D. Pontiroli, M. Riccò, S.R. Clark, D. Jaksch, and A. Cavalleri, Nature **530**, 461 (2016)

[155] A. Cantaluppi, M. Buzzi, G. Jotzu, D. Nicoletti, M. Mitrano, D. Pontiroli, M. Riccò, A. Perucchi, P. Di Pietro, and A. Cavalleri, Nat. Phys. **14**, 837 (2018)

[156] E. Wang, J.D. Adelinia, M. Chavez-Cervantes, T. Matsuyama, M. Fechner, M. Buzzi, G. Meier, and A. Cavalleri, Nat. Commun. **14**, 7233 (2023)

[157] M. Budden, T. Gebert, M. Buzzi, G. Jotzu, E. Wang, T. Matsuyama, G. Meier, Y. Laplace, D. Pontiroli, M. Riccò, F. Schlawin, D. Jaksch, and A. Cavalleri, Nat. Phys. **17**, 611 (2021)

[158] E. Rowe, B. Yuan, M. Buzzi, G. Jotzu, Y. Zhu, M. Fechner, M. Först, B. Liu, D. Pontiroli, M. Riccò, and A. Cavalleri, Nat. Phys. **19**, 1821 (2023)

[159] B.J. Powell and R.H. McKenzie, J. Phys.: Condens. Matter **18**, R827 (2006)

[160] D. Faltermeier, J. Barz, M. Dumm, M. Dressel, N. Drichko, B. Petrov, V. Semkin, R. Vlasova, C. Mézière, and P. Batail, Phys. Rev. B **76**, 165113 (2007)

[161] M. Buzzi, D. Nicoletti, M. Fechner, N. Tancogne-Dejean, M.A. Sentef, A. Georges, T. Biesner, E. Uykur, M. Dressel, A. Henderson, T. Siegrist, J.A. Schlueter, K. Miyagawa, K. Kanoda, M.-S. Nam, A. Ardavan, J. Coulthard, J. Tindall, F. Schlawin, D. Jaksch, and A. Cavalleri, Phys. Rev. X **10**, 031028 (2020)

[162] M. Buzzi, D. Nicoletti, S. Fava, G. Jotzu, K. Miyagawa, K. Kanoda, A. Henderson, T. Siegrist, J.A. Schlueter, M.-S. Nam, A. Ardavan, and A. Cavalleri, Phys. Rev. Lett. **127**, 197002 (2021)

[163] Y.J. Uemura, Phys. Rev. Mater. **3**, 104801 (2019)

[164] M.A. Sentef, A.F. Kemper, A. Georges, and C. Kollath, Phys. Rev. B **93**, 144506 (2016)

[165] D.M. Kennes, E.Y. Wilner, D.R. Reichman, and A.J. Millis, Nat. Phys. **13**, 479 (2017)

[166] M. Knap, M. Babadi, G. Refael, I. Martin, and E. Demler, Phys. Rev. B **94**, 214504 (2016)

[167] M. Babadi, M. Knap, I. Martin, G. Refael, and E. Demler, Phys. Rev. B **96**, 014512 (2017)

[168] A. Nava, C. Giannetti, A. Georges, E. Tosatti, and M. Fabrizio, Nat. Phys. **14**, 154 (2018)

[169] C.N. Yang, Phys. Rev. Lett. **63**, 2144 (1989)

[170] T. Kaneko, T. Shirakawa, S. Sorella, and S. Yunoki, Phys. Rev. Lett. **122**, 077002 (2019)

[171] J. Tindall, B. Buča, J.R. Coulthard, and D. Jaksch, Phys. Rev. Lett. **123**, 030603 (2019)

[172] J. Tindall, F. Schlawin, M. Buzzi, D. Nicoletti, J.R. Coulthard, H. Gao, A. Cavalleri, M.A. Sentef, and D. Jaksch, Phys. Rev. Lett. **125**, 137001 (2020)

[173] Z. Dai and P.A. Lee, Phys. Rev. B **104**, 054512 (2021)

[174] Z. Dai and P.A. Lee, Phys. Rev. B **104**, L241112 (2021)

[175] M.H. Michael, A. von Hoegen, M. Fechner, M. Först, A. Cavalleri, and E. Demler, Phys. Rev. B **102**, 174505 (2020)

[176] F. Gucci, E.B. Molinero, M. Russo, P. San-Jose, F.V.A. Camargo, M. Maiuri, M. Ivanov, Á. Jiménez-Galán, R.E.F. Silva, S. Dal Conte, and G. Cerullo, Nat. Photonics **20**, 266 (2026)

[177] F. Schlawin, D.M. Kennes, and M.A. Sentef, Appl. Phys. Rev. **9**, 011312 (2022)

[178] G. Jarc, S.Y. Mathengattil, A. Montanaro, F. Giusti, E.M. Rigoni, R. Sergo, F. Fassioli, S. Winnerl, S. Dal Zilio, D. Mihailovic, P. Prelovšek, M. Eckstein, and D. Fausti, Nature **622**, 487 (2023)

[179] F. Helmrich, H.S. Adlong, M. Kroner, I. Khanonkin, G. Scalari, J. Faist, A. İmamoğlu, and T.F. Nova, Nature **654**, 361 (2026)

[180] A. Montanaro, V. Plastovets, N. Khatiwada, J. Fiore, G. Jarc, A. Alabbadi, A. Mastropasqua, E.M. Rigoni, S.Y. Mathengattil, S.D. Zilio, F.F. Olsen, F. Novelli, S. Winnerl, M.A. Sentef, D.M. Kennes, A.J. Millis, F. Piazza, and D. Fausti, arXiv:2606.18084 (2026)

[181] H. Zhang, Z. Feng, I.-T. Lu, Z. Li, S. Guo, Q. Shang, D. Luan, M. Panmai, K. Watanabe, T. Taniguchi, A. Rubio, and W. Gao, arXiv:2606.19171 (2026)

[182] F. Appugliese, J. Enkner, G.L. Paravicini-Bagliani, M. Beck, C. Reichl, W. Wegscheider, G. Scalari, C. Ciuti, and J. Faist, Science **375**, 1030 (2022)

[183] I. Keren, T.A. Webb, S. Zhang, J. Xu, D. Sun, B.S.Y. Kim, D. Shin, S.S. Zhang, J. Zhang, G. Pereira, J. Yao, T. Okugawa, M.H. Michael, E. Viñas Boström, J.H. Edgar, S. Wolf, M. Julian, R.P. Prasankumar, K. Miyagawa, K. Kanoda, G. Gu, M. Cothrine, D. Mandrus, M. Buzzi, A. Cavalleri, C.R. Dean, D.M. Kennes, A.J. Millis, Q. Li, M.A. Sentef, A. Rubio, A.N. Pasupathy, and D.N. Basov, Nature **650**, 864 (2026)